Investigation of Materials for Use in High-Temperature, Thin-Film Heaters and Temperature Sensors

by

Samara L. Firebaugh

B.S.E., Princeton University (1995)

Submitted to the Department of Electrical Engineering and Computer Science
in partial fulfillment of the requirements for the degree of

Master of Science in Electrical Engineering

at the

MASSACHUSETTS INSTITUTE OF TECHNOLOGY

June 1997

© Massachusetts Institute of Technology 1997. All rights reserved.

Author.....
Department of Electrical Engineering and Computer Science
May 16, 1997

Certified by.....
Martin A. Schmidt
Associate Professor
Thesis Supervisor

Certified by.....
Klavs F. Jensen
Professor
Thesis Supervisor

Accepted by.....
Arthur C. Smith
Chairman, Departmental Committee on Graduate Students

MASSACHUSETTS INSTITUTE OF TECHNOLOGY

JUL 24 1997 Eng.

LIBRARIES

Investigation of Materials for Use in High-Temperature, Thin-Film Heaters and Temperature Sensors

by

Samara L. Firebaugh

Submitted to the Department of Electrical Engineering and Computer Science
on May 9, 1997, in partial fulfillment of the
requirements for the degree of
Master of Science in Electrical Enginnering

Abstract

Metallizations that can withstand high temperatures are required for many microfabricated systems. In particular, the microfabricated chemical reactor system needs thin metal films for heating and temperature sensing that can withstand prolonged 1000 °C exposure. The current microreactor metallization, 100 nm platinum with a 10 nm titanium adhesion layer, degrades at temperatures > 800°C. This degradation was examined using chemical analysis, scanning electron microscopy, atomic force microscopy, wafer curvature measurements, and high-temperature resistance measurements. While reaction, diffusion and stress contribute to the degradation, the dominant mechanism is hypothesized to be agglomeration. Thicker films and coating layers are demonstrated to increase the lifetime of these films. Suggestions are made for ways to increase the temperature range of the microreactor metallizations.

Thesis Supervisor: Martin A. Schmidt
Title: Associate Professor of Electrical Engineering and Computer Science

Thesis Supervisor: Klavs F. Jensen
Title: Professor of Chemical Engineering and Material Science

Acknowledgements

This work was sponsored by the National Science Foundation. In addition to NSF, there are many people whom I'd like to thank. First and foremost, I would like to thank my advisors, Professor Martin Schmidt and Professor Klavs Jensen, for their guidance and support, without which this thesis would not exist. Dupont, particularly Jim Riley, also provided advice and insight. This thesis also benefitted greatly from the guidance of Professor Carl Thompson and Professor Subra Suresh in understanding some of the materials science issues that the data introduced. I would also like to thank Michele Demarco, who helped to collect and organize the resistance data.

I would like to thank all the members of the MAS and KFJ research groups past and present. In particular, I am grateful to Lalitha Parameswaran and Ravi Srinivasan for sharing their expertise in all manner of things, and Joel Voldman, Mark Sheplak, and I-Ming Hsing for listening to my crazy ideas. I would also like to thank Kathy Vaeth for her help with the AFM, Andrew Gouldstone for his help with the Flexus measurements, and Libby Shaw for her help with the Auger analysis. I am indebted to the MTL staff, particularly Joe Walsh and Octavio Hurtado, for their assistance in training me and aiding with the manufacture and packaging of my samples. Finally , this thesis would not be possible without the self-sacrifice of Agatha, Bertie, Chiswick, Dahlia, Jeeves and Gertrude.

Contents

1. Introduction **13**

1.1 Microfabricated Chemical Reactor Systems 13

1.2 Microreactors at MIT 14

1.3 Semiconductor Industry Metallizations 16

1.4 Thin Film Degradation 17

1.5 Goals of Thesis 20

2. Experiment Design **21**

2.1 Strategy 21

2.2 Sample Fabrication 22

2.3 In Situ Resistance Measurement 24

2.4 Microscopy and Chemical Analysis 29

2.5 Measurement of Stress in Films 30

3. Observations **31**

3.1 Microscopy and Chemical Analysis 31

3.2 Quantifying Degradation with Resistance Measurements 35

3.3 Effect of the Ambient Gas 36

3.4 Tantalum as an Adhesion Layer 38

3.5 Behavior with Capping Layers 39

3.6 Heat Treatment Effect 42

3.7 Thickness Dependence 43

3.8 Films on Membranes 44

3.9 Stress Measurements 48

4. Discussion **52**

4.1 Relating Resistance to Morphology 52

4.2 Oxygen Diffusion and Interlayer Reaction 54

4.3 The Role of Stress 55

4.4 Agglomeration 56

4.5 The Complete Degradation Picture 60

5. Conclusions **62**

Appendix A: Sample Fabrication **65**

Appendix B: Mask Set **70**

Appendix C: Sample Packaging for In Situ Resistance Measurement **75**

Bibliography **79**

Figures

1-1: MIT's Microreactor 15

2-1: Fabrication sequence and metallization pattern 24

2-2: Schematic of Jig 25

2-3: Picture of Jig 25

2-4: Schematic of Test Setup 26

2-5: Picture of Test Setup 27

2-6: Tests Demonstrating Reproducibility 28

3-1: Resistance vs. Temperature for Ti/Pt Film 31

3-2: Appearance of Film Under Optical Microscope After Exposure to 1100°C 32

3-3: SEMs of Ti/Pt Samples Before and After Heating 32

3-4: SEMs of Film Evolution at 900°C 33

3-5: Sketch Derived from Auger Observations 34

3-6: AFM and SEM Images Used for Volume Expansion Estimate 35

3-7: Resistance vs. Time for Ti/Pt Samples at Different Temperatures 36

3-8: 5% Deviation Time vs Temperature for Ti/Pt Samples 36

3-9: Resistance Behavior when Ambient Changed from N_2 to Air 37

3-10: Comparison of 900°C Hold in Air and in N_2 37

3-11: SEMs of Ta/Pt Samples Before and After Heating 38

3-12: Comparison of 900°C Hold for Ta/Pt and Ti/Pt Films 39

3-13: Resistance vs. Temperature for Nitride-Coated Sample 40

3-14: Nitride-Coated Films After Exposure to 800°C 41

3-15: Comparison of 900°C Hold for Uncoated and Alumina-Coated Samples 42

3-16: Optical Microscope Image of Alumina-Coated Film After Heating 42

3-17: Heat Treatment Effect 43

3-18: Resistance vs. Time for Substrate-Supported and Membrane Samples 45

3-19: Optical Microscope Images of Failure in Uniformly-Heated Membranes 45

3-20: Voltage vs. Current for Membrane Metallization 46

3-21: Derived Temperature vs. Power for Membrane Metallization 47

3-22: Degradation in Resistor Metallizations After Self-Heating 47

3-23: Inverse Radius of Curvature vs. Temperature for Nitride-Coated Wafer 48

3-24: Inverse Radius of Curvature vs. Temperature for Nitride/Ti/Pt Wafer 49

3-25: Inverse Radius of Curvature vs. Temperature for Nitride/Ta/Pt Wafer 49

3-26: Estimate of Stress vs. Temperature for Ti/Pt Film 50

3-27: Estimate of Stress vs. Temperature for Ta/Pt Film 51

4-1: Relation of Hole Radius to Resistance 54

4-2: Hole Radius as a Function of Time Interpolated from Ti/Pt Hold Data 58

4-3: Extraction of Surface Diffusion Activation Energy from Data 59

4-3: Illustration of Hypothesized Degradation Process 61

B-1: Backside Nitride Layer Mask 71

B-2: Metal Pattern Mask 72

B-3: Passivation Layer Mask 73

B-4: The Complete Mask Set 74

C-1: Mold for Casting Base Plate 75

C-2: Single Wire Tube After Assembly 77

Tables

2.1 Film Combinations Tested 22

3.1 900°C Lifetimes of Different Material Combinations Tested 44

Chapter 1

Introduction

Thin films are ubiquitous in the semiconductor industry. For example, thin conductive films are often used for interconnections, gates, and contacts in VLSI circuits, and their behavior during manufacture as well as in operation has been extensively examined. Thin films are also used in microfabricated systems, a broader class of devices made with silicon processing techniques which implement functions such as environment sensing, material transport, or mechanical actuation. Some of these systems experience high temperatures not only in fabrication but also in operation. Materials must be selected and prepared for endurance during lengthy exposure to high temperatures and thermal cycling. This thesis looks at the thin platinum films used in a microfabricated chemical reactor system, but the observations made here can be applied to a variety of microfabricated systems.

1.1 Microfabricated Chemical Reactor Systems

This investigation of thin platinum films is part of the development of a silicon-based chemical reactor system. The concept of the microchemical system represents a paradigm shift for the chemical industry. In conventional production, chemicals are synthesized in meter-scale reactors. If only small amounts are required, as in the case of an intermediate reagent, the chemical is made in bulk and then stored or shipped to where it is needed. The typical R&D to market cycle has two distinct stages. First, a small-scale

laboratory reactor is studied and optimized, then the full-scale reactor is built. Because parameters such as selectivity and conversion do not simply scale with reactor volume, the construction of the industrial scale reactor involves another round of investigation and optimization.

A microfabricated reactor system would consist not of one massive reactor chamber, but of hundreds of small reactors operating in parallel. This has two essential differences from conventional reactor systems: increased modularity and higher surface to volume ratios. Once one microreactor is optimized, the system can be scaled up by simply adding reactors in parallel to produce the volumes needed. In addition to allowing flexibility in meeting a fluctuating demand, this allows point-of-use development: intermediates can be made on location in the quantities needed, rather than being stored or shipped. Eliminating the need for storage or shipping of dangerous chemicals also increases the safety of these systems. The increased surface-to-volume ratio offers another safety advantage. Heat can be quickly removed from the reactor chamber, and the wall-quenching of free-phase radicals is enhanced. Because of these safety advantages, highly-exothermic partial oxidation reactions are a good candidate for microreactor implementation.

Many groups are working on microfabricated systems. Dupont has run hazardous reactions in an externally-heated, silicon wafer-bonded stack with microchannels.[1] Hönicke et al. have also demonstrated reactions in externally-heated microchannels[2,3], and Ehrfield et al. have microfabricated static mixers, heat exchangers and chemical reactors using LIGA and photo-etched glass.[4] Heat-exchangers and combustor-evaporators have also been made on silicon wafer stacks.[5]

1.2 Microreactors at MIT

At MIT, Srinivasan et al.[6] have built a reactor for gas-phase, catalytic, partial-oxidation reactions. The reactor consists of a T-shaped channel etched through a silicon

wafer, capped on the top by silicon nitride and on the bottom by an aluminum plate. 100 nm platinum lines, adhered to the top of the silicon nitride by 10 nm of titanium, are used as resistors for ohmic heating and temperature sensing. Platinum on the underside of the membrane acts as a catalyst. Reactants enter through inlet holes in the aluminum plate, mix at the head of the T, react along the catalyst, and exit at an outlet hole in the plate at the bottom of the T.

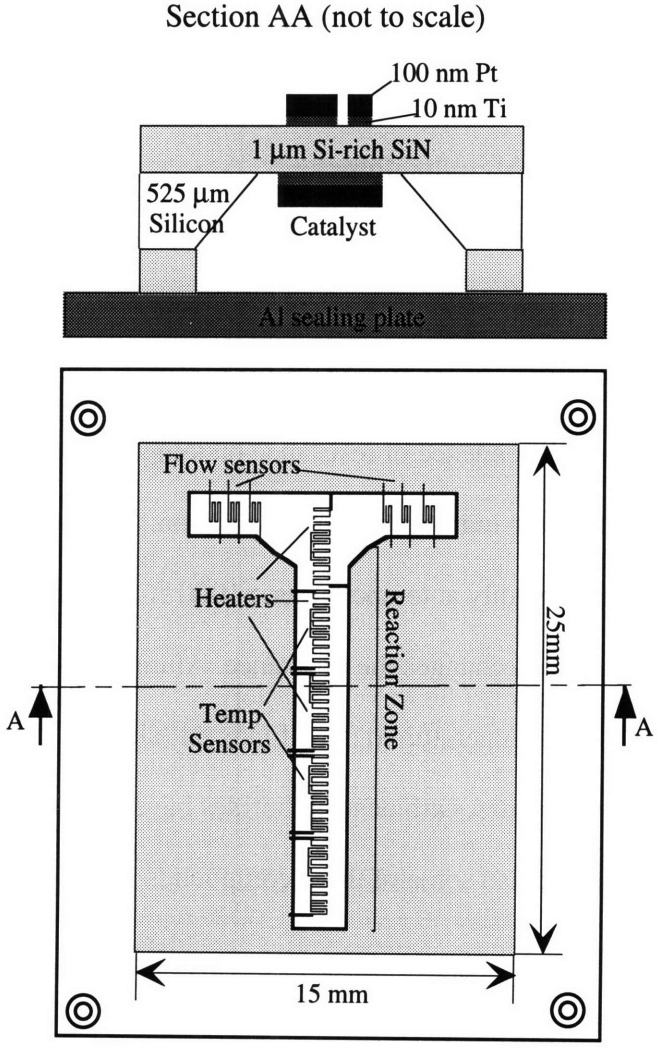

Figure 1-1: MIT's Microreactor

The partial oxidation of ammonia was used to demonstrate functionality and characterize the effects of temperature and flow rate on the conversion and selectivity. While this test reaction runs at ~600°C, many commercially-relevant partial oxidation

reactions take place at higher temperatures, ~1000 °C. The current reactor system, however, cannot exceed 700°C in operation, at which point the nitride membrane fractures. Also, extended use at high temperature transforms the surface morphology of the platinum films, and alters the temperature dependence of film resistances. In future generations of the microreactor, engineering the geometry of the reactor so as to lessen the effect of stress should increase the robustness of the membrane. But for high temperature operation, the thin film degradation phenomena must also be avoided. The work of this thesis is to identify the cause of the degradation, and then to identify ways to solve the problem.

1.3 Semiconductor Industry Metallizations

A variety of materials are used for metallizations in silicon micromachining, including polysilicon, aluminum, gold, silicides, refractory metals, nitrides, carbides, borides and combinations of these materials.[7] For this application, we require a metallization for which the dependence of resistance on temperature remains the same over many thermal cycles and during high-temperature operation.

Polysilicon oxidizes readily at temperatures >1000 °C, and it exhibits large amounts of grain growth which changes the resistance. Aluminum and gold both have low melting points relative to the temperature range of interest (aluminum melts at 660°C, and gold at 1064°C). Silicides, nitrides, carbides and borides have high melting points, but they are more difficult to deposit. Also some of these compounds react with oxygen at high temperatures.

Refractory metals such as platinum, tungsten and irridium are potential metallization candidates because of their high melting points and ease of deposition. Often, however, these metals have poor adhesion to glassy substrates. A thin layer of a readily-oxidized metal such as titanium or chromium is required to promote adhesion. This layer

often also functions as a barrier to silicide formation. Tantalum has also been used as an adhesion layer.[8]

In the first generation of microreactor, platinum was chosen for the metallization because of the high melting point (1769 °C), ease of deposition, resistance to oxidation, and because platinum was already a part of the system as the catalyst. Titanium was chosen as the adhesion layer material because its thermal expansion coefficient is similar to that of platinum. The thermal expansion coefficient of platinum is 8.8 ppm/K, while the coefficient for titanium is 8.6 ppm/K.[9] However, the thermal expansion coefficient of silicon-rich silicon nitride is 1.6 ppm/K[10], so there will be large compressive stresses in the films at high temperatures. Another potential problem with the Ti/Pt metallization is that titanium and platinum form a eutectic at 840°C, and titanium and silicon form a eutectic at 865 °C.[11] Therefore, it might be advantageous to try tantalum as an adhesion layer instead of titanium. Its lowest eutectic temperatures are 1635 °C and at 1400 °C with platinum and silicon, respectively. Also, since its thermal expansion coefficient is 6.3 ppm/K, it might reduce the stress in the platinum by creating a graded change in expansion coefficient.

1.4 Thin Film Degradation

A variety of degradation phenomena have been observed in thin metal films. They include: interlayer diffusion and reaction, stress-induced morphological changes, electromigration and surface-diffusion-driven agglomeration.

Olowolafe et al.[12] have observed interdiffusion in Pt/Ti bilayers deposited on top of SiO_2/Si and TiN/Ti/Si layers. After heating films of 2000 Å Pt/ 1000Å Ti and 930 Å Pt/ 1000 Å Ti for thirty minutes at 600 °C and at 800 °C in oxygen and in nitrogen, the surfaces roughened visibly. X-ray diffraction analysis revealed the existence of Pt_3Ti, TiO_2, and Ti_5Si_3 phases in the annealed sample in addition to Pt and Ti. The author suggests that

Ti and O_2 are diffusing through grain boundaries in the Pt layer and reacting until the Ti is consumed.

Park et al.[13] have also observed interdiffusion and reaction in Pt/Ti layers. They annealed 80 nm Pt/ 70 nm Ti/ SiO_2/ Si samples in O_2 at a variety of temperatures. They observed oxidation and interdiffusion at samples annealed at temperatures above 500 °C, and Pt hillocks above 600°C. Fox et al.[14] observed grain growth, and rounding of grain surfaces at 200 nm Pt/ 20 nm Ti/ SiO_2/ Si films which had been annealed at 650 °C for 20 min. In addition to the grain growth, they also observed two types of defects: 150 nm hillocks, and dark regions postulated to be the result of alloy or oxide formation.

Sreenivas et al.[15] studied the effect of Ti layer thickness on Pt/Ti/SiO_2/Si structures that underwent rapid thermal anneals at temperatures ranging from 200 to 800 °C. The Ti layer readily oxidized in all cases. Post-anneal adhesion problems were observed for films with 10 nm Ti adhesion layers, while TiO_{2-x} formed in the Pt grain boundaries of the films adhered with 100 nm Ti, eventually encapsulating the Pt layer. Better stability was achieved by depositing Pt films at high temperature.

Several groups have reported hillock formation in platinum films[16,17,18]. The large thermal expansion mismatch between silicon nitride and the Pt/Ti might result in large compressive stresses at high temperatures, which the film can relieve through hillock formation, as was observed by Murakami[19] for lead films. Hillock growth occurs as a result of differential relaxation rates between a grain in a polycrystalline film and its surroundings. This sets up a stress gradient, which induces mass to flow along the substrate/film interface, pushing the relaxed area out at the base to form a hillock.[20,21] Mechanical stress-induced degradation is well-documented for the aluminum films used in VLSI circuits, where stress from the thermal expansion mismatch between silicon and aluminum leads to hillocks, voids, and cracks.[22]

Another phenomena to consider is electromigration, mass flow driven by the interaction between the atoms of a conductor and the direct current of electrons flowing through it. There are two effects at work that move the atoms: the electrostatic interaction between the electric field and the ionic core of the atoms, and the friction force between the ions and the flowing charge carriers. In metals the latter force, sometimes called "electron wind," is dominant. There is very little work on electromigration in platinum thin films. D'Heurle and Ho, however, have reviewed electromigration studies of aluminum, gold, silver, tin, copper, cobalt, magnesium, indium and lead thin films[23]. Electromigration failures typically occur in these thin films when high current densities (10^5 to 10^7 A/cm^2) are present at moderate temperatures relative to the material melting point ($0.3\ T_m < T < 0.7\ T_m$). In this work, we are working at temperatures between 50% and 70% of the melting temperature of platinum. By using current densities of 10^2 A/cm^2 for sensing, we should therefore avoid electromigration effects. The higher current densities (10^3-10^4) used for heating might display some electromigration effects, however, but they are not considered in this thesis.

Yet another mechanism of thin film degradation is agglomeration, the decomposition of a thin continuous film into a collection of beads. The process is driven by the high surface to volume ratio of thin films. Surface diffusivity, which is exponentially-dependent on temperature, acts to reduce the surface area through capillarity.[24] The process is a nucleation and growth process. Defects, pinholes or thermal grooving at a grain boundary[25] must first establish a hole greater than a critical radius, which is determined by film thickness and wetting angle.[26] Stress can hasten the formation of a hole by differentially thinning the material. Once the critical radius is achieved, the hole will grow until the film is transformed into a collection of unconnected, hemispherical islands. In general, agglomeration is enhanced by temperature and reduced by thickening films and by

increasing the adhesion between the film and the substrate. Some studies indicate that stress enhances agglomeration,[27,28] but the effect of stress has not been measured quantitatively.

1.5 Goals of Thesis

Working towards the general goal of expanding the temperature range of operation for the microreactor system, this thesis will explore the high temperature behavior of the metallization materials of the microreator. The goal of the thesis is to accomplish the following:

1. Characterization of the current system's behavior in the temperature range of 800 to 1100 °C.
2. Identification and exploration of the mechanisms responsible for degradation of the microreactor metallization.
3. Identification of material combinations that will increase the microreactor's temperature range of operation.

Chapter 2

Experiment Design

The primary role of the metallizations under investigation is to resistively sense temperature, and to ohmically heat the reactor chamber. As a result, the morphology is not as important as the temperature dependence of the resistivity. For sensing, the temperature dependence must be independent of thermal history. Our characterization, therefore, focused on the resistance behavior of the films. Scanning electron microscopy (SEM), atomic force microscopy (AFM), Auger electron spectroscopy (AES) and wafer curvature measurements were also used to supplement our understanding of the degradation mechanism.

2.1 Strategy

Measuring the resistance of the films while they are heated will allow us to quantitatively determine the conditions under which degradation occurs. There are many variables to consider: temperature, time, film thickness, choice of barrier layer, environment, the effect of capping layers, the presence or absence of a membrane, and uniform vs. ohmic heating of films. It seems rational to begin with uniformly-heated, substrate-supported metal patterns, and vary only the temperature and time in order to quantify the degradation mechanism.

Examining the effect of changes in the other variables will then supplement our qualitative understanding of the mechanism. Looking at two environments, air and

nitrogen, will allow us to observe the effect of oxygen. Looking at a second thickness, different adhesion layer material, or at the effect of a capping layer will also enhance our understanding of the degradation. Finally, looking at films on membranes, where the thermal mismatch stress is partially relaxed by membrane deflection, will allow us to see the effect of stress on the degradation phenomena. Table 2.1 shows the matrix of variable combinations; those tested are marked by a check.

Materials	Substr. Films in Air	Substr. Films in N_2	Un-Patterned Membs. unif. heating	Patterned Membs. unif. heating	Patterned Membs. nonunif. heating
10 nm Ti/100 nm Pt	√	√	√	√	√
10 nm Ti/ 100 nm Pt/ 300 nm Al_2O_3	√				
10 nm Ti/ 100 nm Pt/ 100 nm Si_3N_4	√				
10 nm Ta/ 100 nm Pt	√				
20 nm Ta/ 100 nm Pt	√				
10 nm Ta/ 200 nm Pt	√				
10 nm Ta/ 400 nm Pt	√				

Table 2.1: Film Combinations Examined

Optical microscopy, Auger, SEM and wafer curvature analysis were also used to explore the pheonemena. Results from earlier tests were used to guide later tests: for example, the observation of increased lifetimes in an oxygen-poor atmosphere motivated the testing of nitride- and alumina-coated samples.

2.2 Sample Fabrication

Four types of samples were made: patterned metal films without membranes, patterned metal films with membranes, unpatterned metal films with membranes, and patterned metal films without membranes and with oxidation barrier layers. The process is as similar as possible to that of the microreactor fabrication, so that the metal layers studied here had the same history as the films in the microreactor.

The pattern, shown in figure 2-1, has eight resistors and one large central pad to make chemical analysis and microscopy easier. Each of the resistors has four bond pads to

facilitate a four point resistance measurement, which will minimize the effect of contact resistance. Three of the resistors mimic the three geometries of resistors used in the microreactor: meandering, 50 μm-wide lines for heating, and two types of meandering, 10 μm-wide lines for temperature sensing and anemometry. There are also straight line resistors with the same width of each of these types. Finally, there is an additional heater resistor and sensor resistor, where the sensor resistor is interwoven with the heater resistor as they are configured in the microreactor.

The fabrication of all the samples (illustrated in figure 2-1, see appendix A for details) began with four-inch, <100> silicon wafers, coated front and back with ~1 μm silicon-rich silicon nitride. The nitride on the backside of the membrane wafers was patterned and etched as a mask for membrane release. Photoresist was deposited on the front side of the patterned metal wafers and patterned through image reversal, with infrared alignment being used on the membrane wafers to align the metallization to the membranes. The metal layers were evaporated onto the wafers without breaking vacuum between the adhesion layer and the platinum layer. After the metal was lifted off in the undesired areas, the wafers were sintered at 650°C in nitrogen for one hour. The purpose of the sinter step in the microreactor fabrication sequence is to anneal defects in the films.[29]

Membrane wafers were etched in potassium hydroxide (KOH) to release the membranes. When a passivating layer was to be added, it was deposited on the wafers after the sinter. In this work, nitride was deposited on some samples using plasma-enhanced chemical vapor deposition (PECVD), and alumina was evaporated onto other samples. The passivation layer was then removed over the bond pads via reactive ion etching (RIE) for the nitride, and with a dip in buffered oxide etchant (BOE) for the alumina.

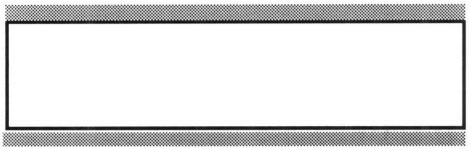

1) 1 μm Si-rich nitride deposited on front and back of wafer

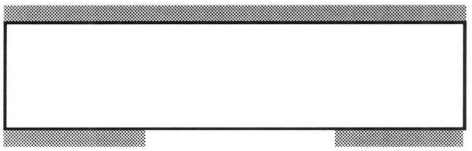

2) On membrane wafers, the backside nitride patterned

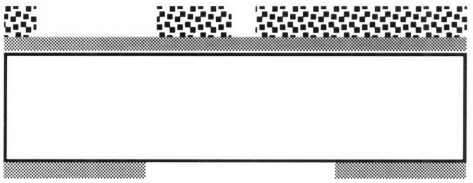

3) On patterned wafers, photoresist (PR) is patterned on front side for metal lift-off

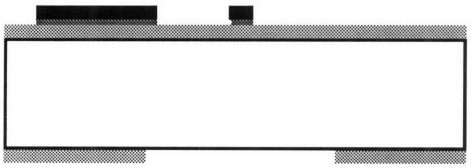

4) 10 nm Ti (or Ta) and 100 nm Pt deposited by e-beam. PR removed. Wafers sintered at 650 °C for 1 hr.

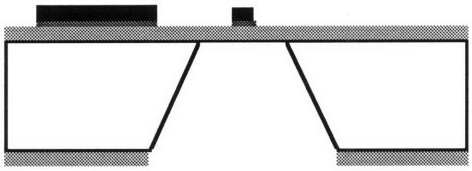

5a) For membrane wafers, membrane released by KOH etch

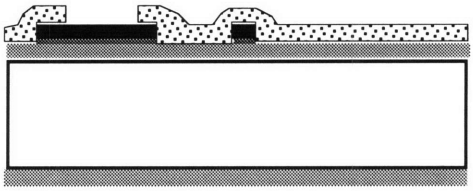

5b) For wafers with an oxidation barrier layer, coating material was deposited and then patterned for contact holes.

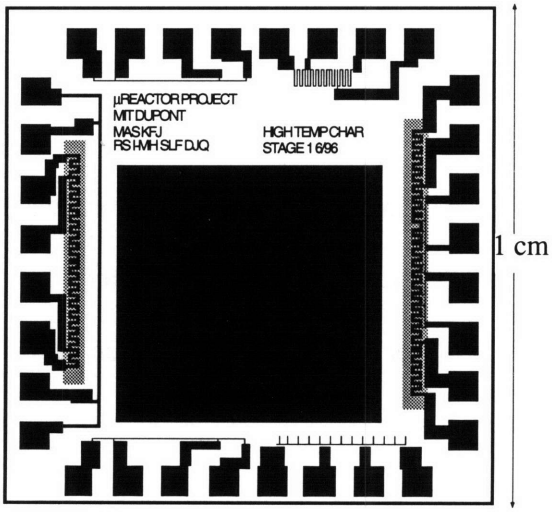

Figure 2-1: Fabrication Sequence and metallization pattern

2.3 In Situ Resistance Measurement

The most difficult aspect of the in situ resistance measurement is making the electrical connections from the external measurement circuit to the chip in the furnace. This was accomplished with a custom-made alumina jig. The chip sits on a base plate made out of castable alumina ceramic and formed in a wax mold. Wires made from Kanthal-D®[30], an iron-chromium-aluminum alloy designed to withstand high temperatures for long periods of time, were run through foot-long, 1/8"-diameter alumina tubes attached to the

base plate with high-temperature cement. The ends of the Kanthal® wire were spot welded to small pieces of platinum foil. Wedge bonding with pre-annealed, 25 μm-diameter platinum wire connected the foil to the contact pad. A K-type (chromel/alumel) thermocouple was also brought in through alumina tubes, and attached so that the junction was close to the sample. For details on the jig construction, see appendix C. The jig is shown in figures 2-2 and 2-3.

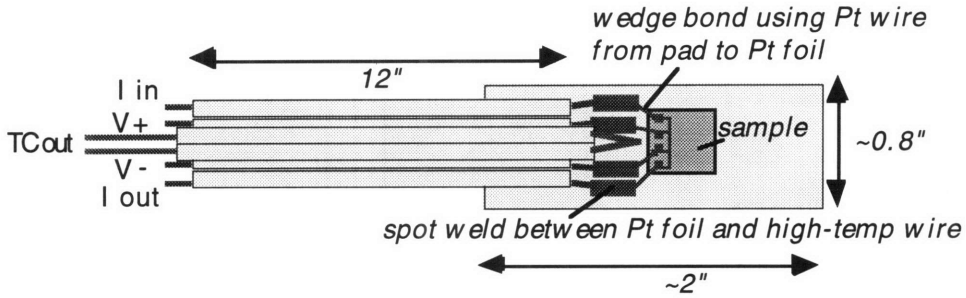

Figure 2-2: Schematic of Jig

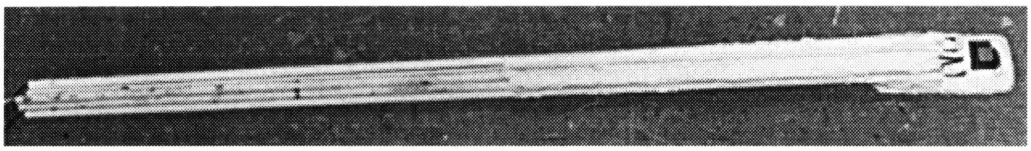

Figure 2-3: Picture of Jig

Using the alumina tubes as a handle, the jig was placed in a one-inch diameter quartz tube, lying in a tube furnace which was controlled by a programmable controller via a solid-state relay. The temperature used for furnace control was taken from the thermocouple attached to the jig in order to achieve accurate control of the film temperature. The ambient was controlled by flowing nitrogen or compressed air through the tube at 150 mL/min. This flow, with the addition of a vent box which sat in front of the entrance of the tube and was attached to the vent, caused external air that entering through the box with the connecting wires to be sucked into the vent instead of entering the tube. A schematic of the test apparatus is shown in figure 2-4.

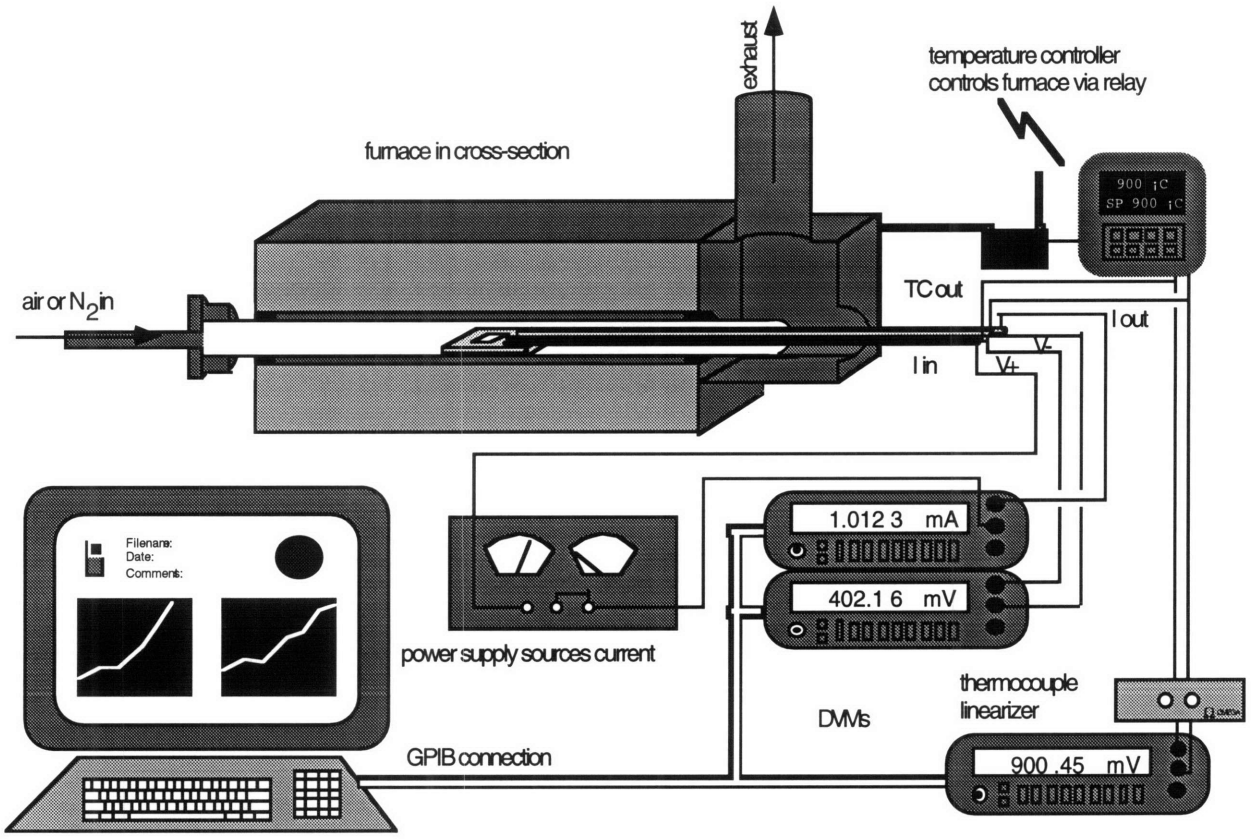

Figure 2-4: Schematic of Test Setup

The temperature profile of the tube was measured at 900 °C without the jig in place and found to vary by less than 1° over the center 5 cm of the tube. Since the silicon is a far better thermal conductor than air, the temperature profile over the 1 cm sample should be even more uniform. With the thermocouple placed just above the chip, therefore, we can expect reasonable accuracy in the temperature measurement.

The four-wire ohm resistance measurement was accomplished using a power supply and two digital multimeters (DVM). Sensing currents of about 1 mA, which corresponded to a current density of 200 A/cm^2 in the 50 μm-wide lines, were forced through the test resistor through the outer two contacts and measured by one multimeter. The other multimeter read the voltage off of the inner two contacts. The voltage for the straight line resistor was typically ~110 mV at room temperature. Figure 2-5 shows a photograph of the test set up while it was operating at ~600°C with a low current.

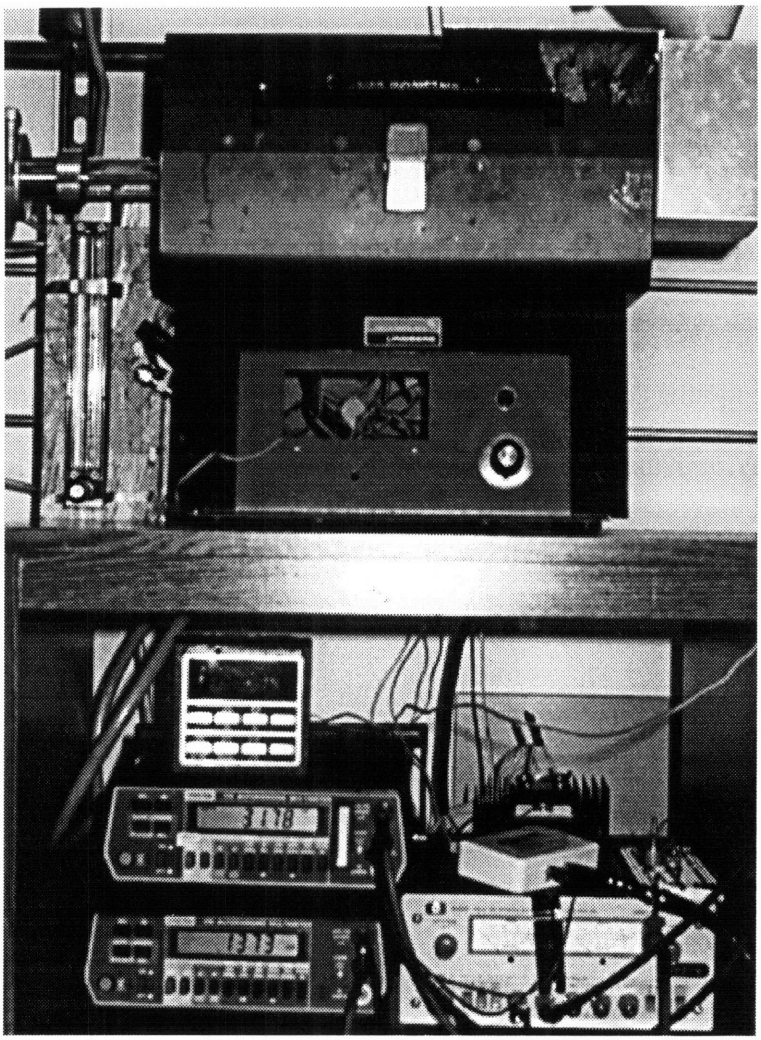

Figure 2-5: Picture of Test Setup

Because of the work function difference, there was a temperature-dependent voltage drop at the junction between the Kanthal® wire and the platinum foil which was examined as a source of error. At 926 °C, the voltage difference that resulted from the the work function disparity was measured to be 11 mV. However, all of the voltage measurements were symmetric with junctions on both ends of the sample resistor. As long as the junctions were at the same temperature, the voltage differences should cancel out. This was tested by spot welding two pieces of Kanthal® wire to a strip of Pt foil and placing it in the furnace. The total voltage drop was measured to be negligible and not dependent on temperature.

The current, voltage and temperature were read by a PC using LabVIEW®[31]. Temperature was translated into a voltage with a thermocouple linearizer. Both an A/D card and GPIB were used for reading the instruments. When A/D was used, voltages were fed directly into the board. The current was forced through a known resistor in addition to the sensing circuit, and the voltage over the resistor was read by the A/D card and translated back into the current value. When GPIB was used, the output was taken directly off of the DVMs, and an additional DVM was used to read the temperature. The resistance was then found by dividing the voltage by the current.

The accuracy of the system was tested by monitoring the resistance in the 22-600°C temperature range. The results are shown in figure 2-6. Below 400 °C, the resistance responds linearly to temperature change, but from 400-600 °C, the response drops away from the linear fit. This data is consistent with observations made by Srinivasan et al. for the microreactor metallizations.[29]

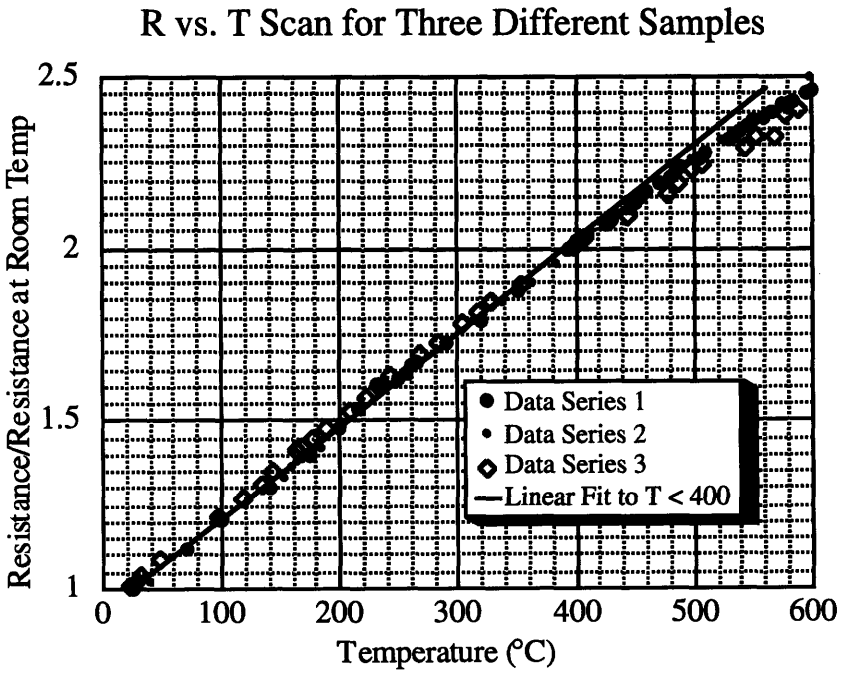

Figure 2-6: Tests Demonstrating Reproducibility

2.4 Microscopy and Chemical Analysis

SEM, optical microscopy and AFM were used to observe the visual appearance of the surface. Chemical analysis was carried with AES. In SEM, an electron beam is scanned over a surface as the backscattered electrons (or secondary electrons) are collected and translated into an image. Conducting materials will generally produce more backscattered electrons than insulators, although a phenomenon called "charging" sometimes occurs for insulators. Charging occurs when the impinging electron beam causes static charge to build up on the insulator surface, resulting in a glow in the region. In this work with SEM, the platinum imaged well, but in areas where oxidized titanium or silicon nitride were exposed charging occured. It did not, however, substantially interfere with the investigation.

AFM uses the attractive van der Waals force, which exists between any pair of closely-spaced atoms, to map the contours of a surface. The tip of a cantilever is brought very close to the surface so that there is an attractive force between the cantilever tip and the sample. The resonance frequency of this cantilever depends on the gradient of that force, which is a function of the separation between the tip and the sample. As the cantilever is rastered over the sample, the height of the tip is adjusted so as to maintain a constant resonance frequency. The tip deflection, detected optically, is then translated into a map of the surface.[32] Features with sudden, relatively large height changes can be difficult to image, because the rate of change is at the limit of the feedback loop. This phenomenon resulted in some noise in the AFM images shown in section 3.1.

AES also relies on the detection of electrons emitted as the result of an impinging electron beam. However the electrons of interest are not the backscattered or the secondary electrons, but rather "Auger" electrons. These electrons have energies characteristic of the separations between core levels, and therefore act as fingerprints for the elements on the

surface. It is a surface-analysis technique because the mean free path of Auger electrons in a typical solid ranges from 4 to 20Å.[33] Depth profiling is achieved by alternating ion sputtering with Auger scans for composition. A material must be conductive in order to be analyzed by AES. This was a problem for analyzing the composition of the areas in the degraded films which had reacted to form insulating material.

2.5 Measurement of Stress in Films

The stress in the metallization was measured indirectly by using a Tencor[34] Flexus® 2908 to measure wafer curvature as a function of temperature. For films which are very thin with respect to their supporting substrates, the wafer curvature can be used to measure stress in the films. A full derivation of the relationship between radius of curvature and stress is given by Flinn et al.[35] The equation for a single film on a substrate is as follows:

$$\sigma_f = (E_s t_s^2)/[6(1-\nu)t_f R] \qquad (1)$$

where σ_f is the stress in the film, E_s is the young's modulus of the substrate, t_s is the substrate thickness, t_f is the film thickness, ν is the Poisson's ratio of the substrate, and R is the measured radius of curvature. In multilayer films, the stress of a particular film is found simply by substituting the change in 1/R with and without the film for 1/R in the formula.

In this work, the curvature of a plain wafer with nitride was measured in addition to the curvature of nitride/Ti/Pt and nitride/Ta/Pt coated wafers. Nitride/Ti and nitride/Ta wafers could not be measured for meaningful analysis of the stress in the platinum layer alone, because the chemical composition of titanium and tantalum changes without the platinum layer to retard oxidation.

Chapter 3

Observations

As is shown in figure 3-1, the resistance of the metallization is well-behaved up to ~900 °C, but then increases rapidly with additional temperature rise. The resistance change appears to be related to hole formation and growth in the films. Testing explored both the resistance variation and the morphological change.

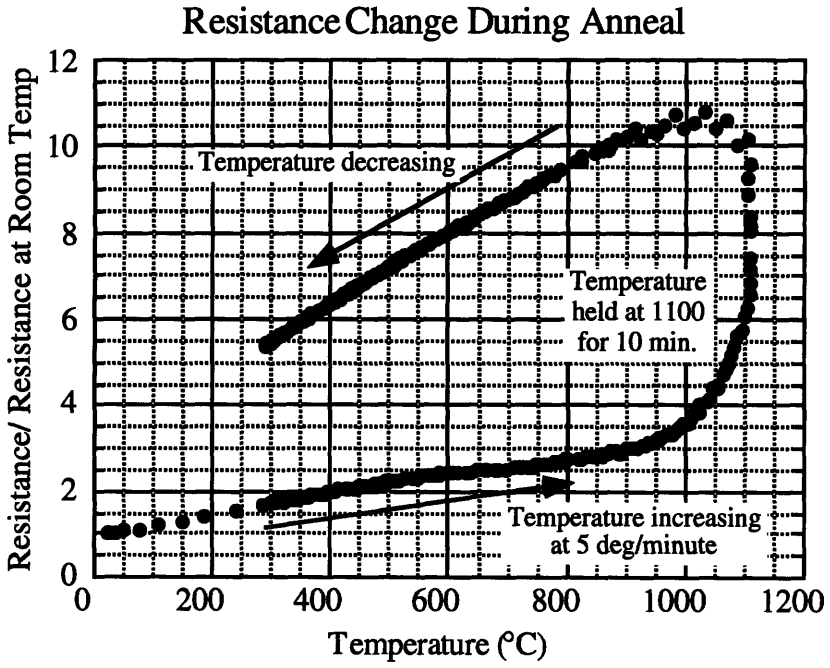

Figure 3-1: Resistance vs. Temperature for Ti/Pt Film

3.1 Microscopy and Chemical Analysis

To the naked eye, the metal films appear to dull after high temperature operation. Optical microscopy reveals a roughened, hole-riddled surface (see figure 3-2). Further

inspection at higher magnification with SEM indicates that the film is segregating into islands (see figure 3-3), and that there is structure in the holes.

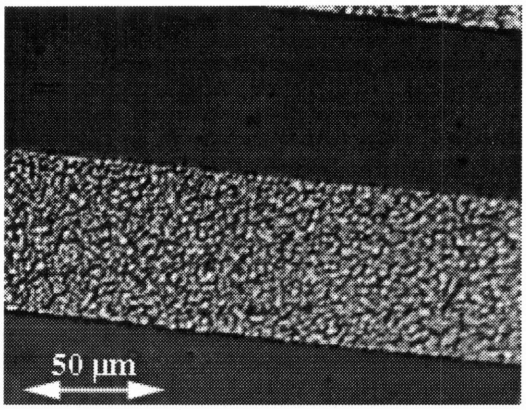

Figure 3-2:Appearance of Film Under Optical Microscope After Exposure to 1100 °C

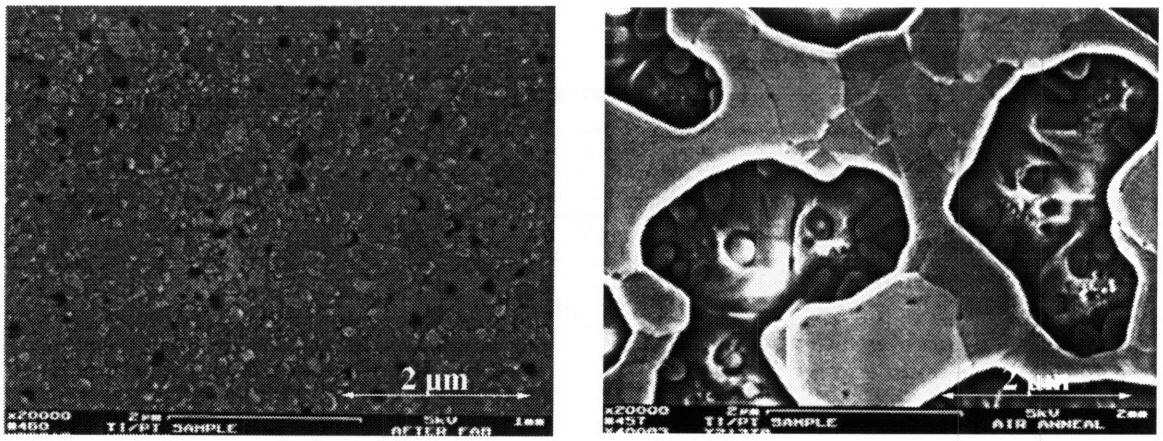

A) After sample fabrication *B) After exposure to 1100°C in air*

Figure 3-3: SEMs of Ti/Pt Samples Before and After Heating

The evolution of the morphology was studied by looking at samples that had been exposed to heat treatment of 900 °C for varying lengths of time (figure 3-4). Randomly-distributed holes with an average diameter of approximately 300 nm formed as the sample was being brought up to temperature. The holes then grew unevenly with increased exposure, joining in places to form islands of material.

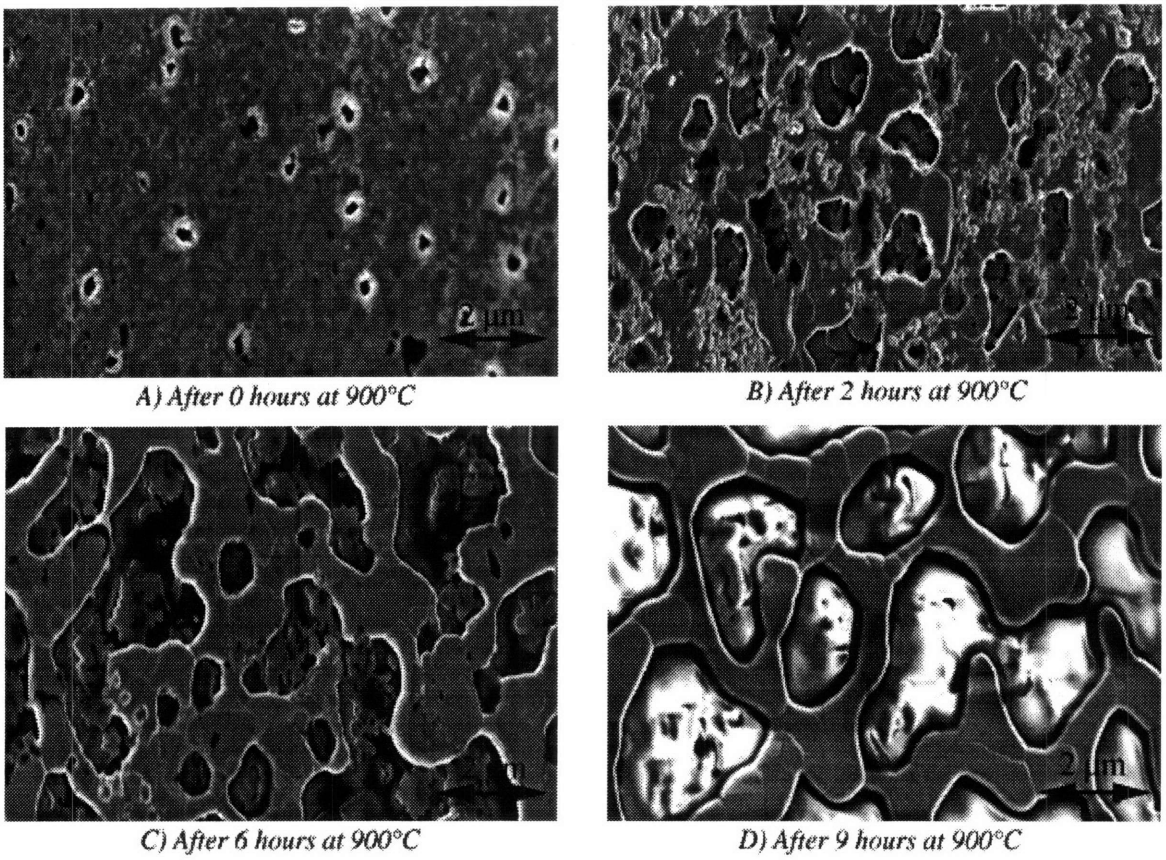

A) After 0 hours at 900°C

B) After 2 hours at 900°C

C) After 6 hours at 900°C

D) After 9 hours at 900°C

Figure 3-4: SEMs of Film Evolution at 900 °C

Auger analysis was used to analyze the composition of the films after heating. Sputter rate was calibrated to depth by sputtering through an untreated sample with known film thicknesses. In examining these untreated films, oxygen was discovered at the titanium-platinum interface. This was probably incorporated during the film evaporation. Even at pressures of 10^{-7} torr, there is enough oxygen in the chamber to be incorporated into the titanium[36]. In fact, titanium is often used in vacuum systems to getter oxygen.

The Auger analysis revealed that the bulk of the coalesced structures is platinum, while oxygen and titanium were found in the valleys. Sputtering through the platinum hills, some silicon was found as the crater approached the nitride underneath the films, revealing the formation of a platinum silicide. Surprisingly, no titanium was found between the platinum and the nitride. This could, however, be the result of charging obscuring the

measurement as the conducting layer is lost. Figure 3-5 shows a sketch of the material cross-section, derived from the Auger findings.

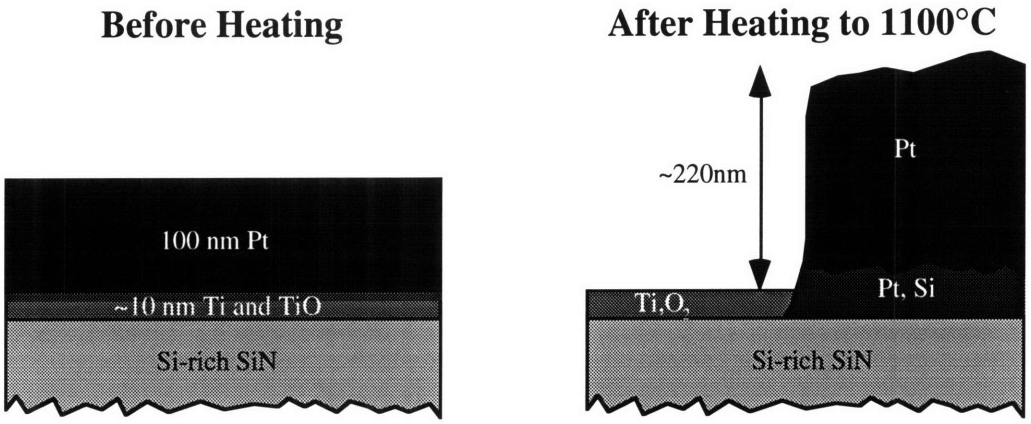

Figure 3-5: Sketch Derived from Auger Observations

Cross-sections of an Atomic Force Microscopy (AFM) image of a sample that had been heated to 1100 °C in air and held there for ten minutes revealed that the average height of the platinum in the ridges had more than doubled to ~220 nm. The surface area of the platinum film after heating was estimated from an SEM. The surface area was found to have been reduced to about 45% of its original value. The AFM and SEM are shown in figure 3-6. (The scale of the AFM photo is misleading because it includes the effects of tip overshoot around the edges of the features; the valleys are actually at a height of ~170 nm on this scale.) Combined, these numbers indicate that the volume of the platinum remained constant during heating, which is consistent with our AES observation that the bulk of the platinum did not undergo chemical reaction.

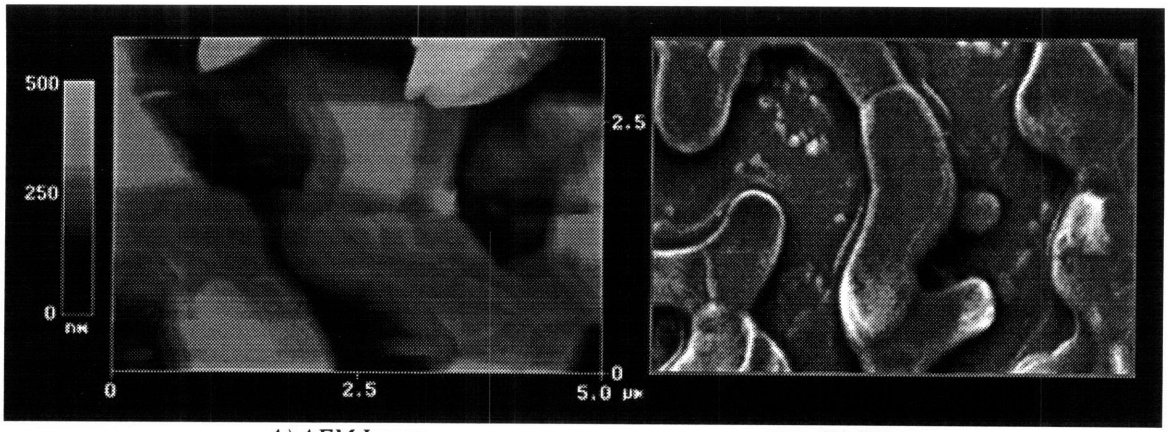

A) AFM Image *B) SEM Image*

Figure 3-6: AFM and SEM Images Used for Volume Expansion Estimate

3.2 Quantifying Degradation with Resistance Measurements

There are too many variables in the resistance/temperature scan to make quantitative measurements easy. A better method is to hold temperature fixed, and to monitor the resistance change over time. Therefore, a series of tests were carried out where the sample was brought up to a set temperature at 10 deg/min, and then held as the resistance was measured every minute. The time required for a five percent deviation in the resistance was recorded as indicative of the lifetime of the metallization at that temperature. There were many sources for error in these tests, including LabVIEW® errors which sometimes resulted in inaccurate time measurement, scratches or defects on the sample which acclerated film degradation, and a drift (over months) of the temperature controller's reading of the temperature. Eliminating data gained in runs with an incorrectly calibrated controller, or in runs with delays from computer data aquisition errors, the error in the time measurements ranged from 3-13%. As expected, the resistance change rate increased with temperature (figures 3-7 and 3-8). Hold temperatures ranged from 800°C to 900°C. The narrow range was chosen because at lower temperatures, change took place too slowly to be time efficient, and at higher temperatures the resistance had already begun to deviate by the time the hold temperature was reached.

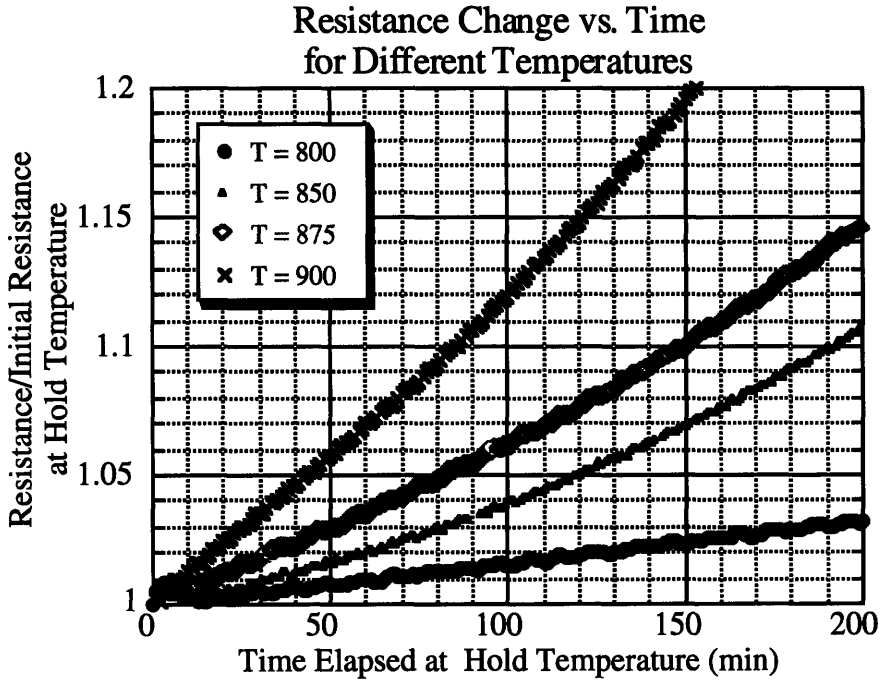

Figure 3-7: Resistance vs. Time for Ti/Pt Samples at Different Temperatures

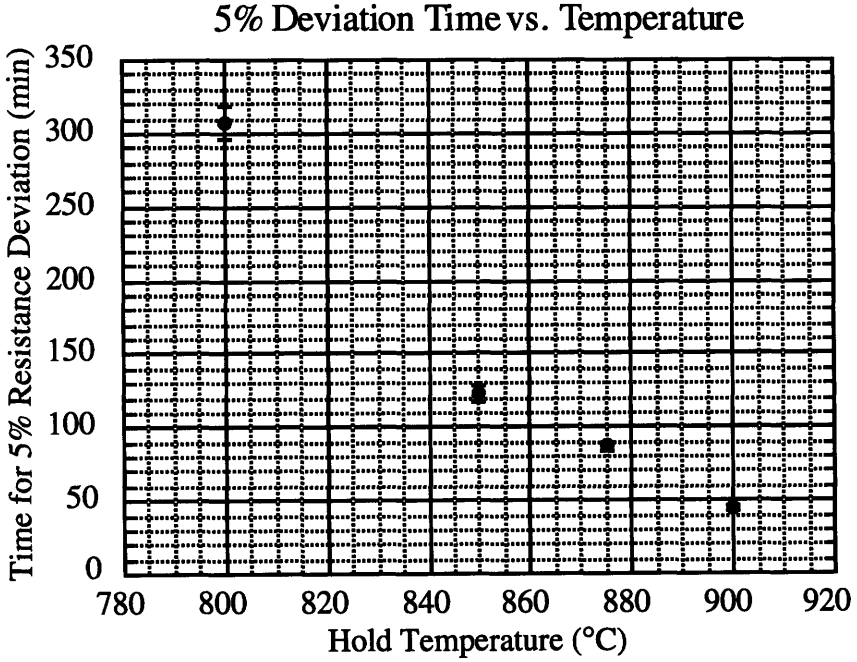

Figure 3-8: 5% Deviation Time vs. Temperature for Ti/Pt Samples

3.3 Effect of the Ambient Gas

Previous work[12,13,15] indicates that oxygen affects the degradation of Pt/Ti films. This effect was observed here by comparing films annealed in air to films annealed in nitrogen. As is shown in figure 3-9, the degradation rate of a film initially brought up to

temperature and held at 900°C in nitrogen was observed to increase when the environment was switched to air.

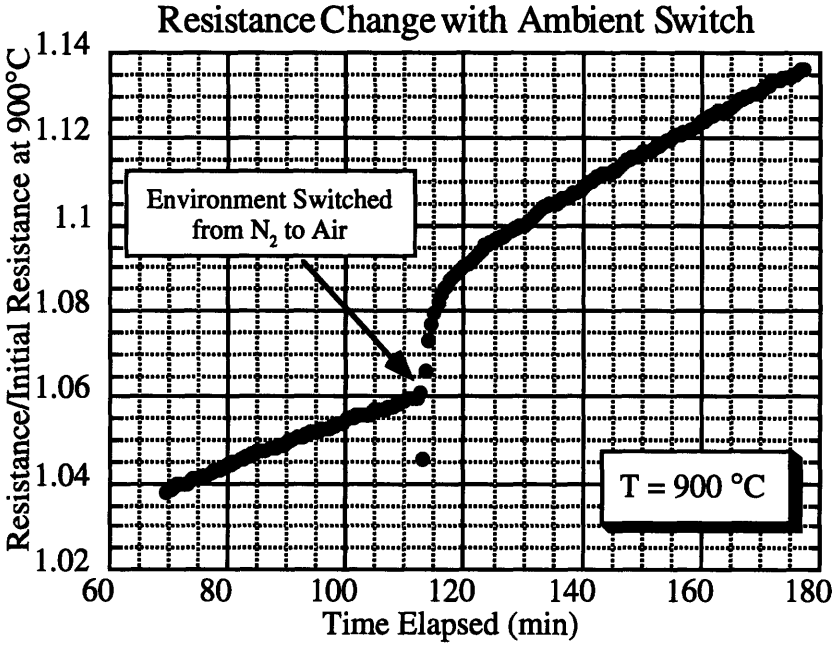

Figure 3-9: Resistance Behavior when Ambient Changed from N_2 to Air

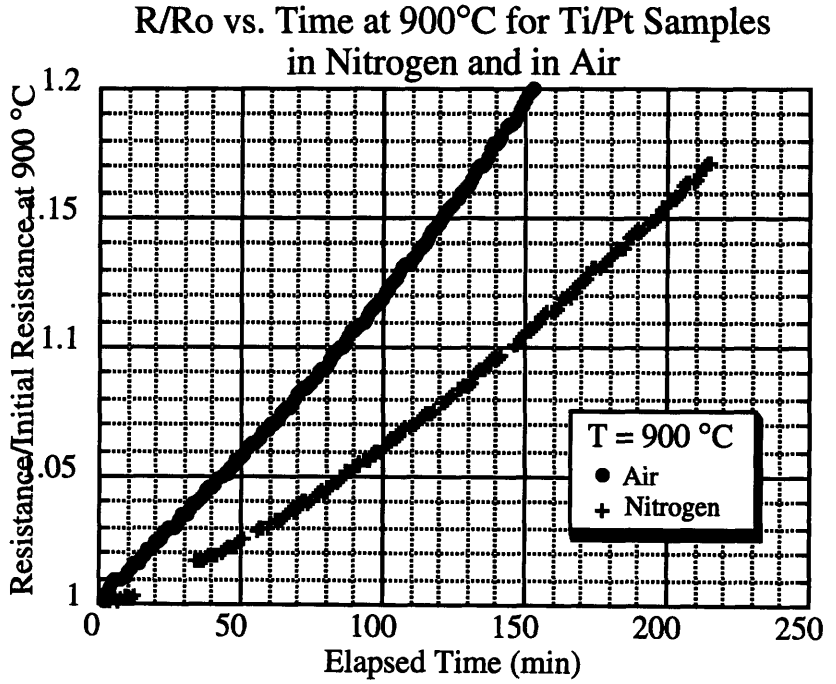

Figure 3-10: Comparison of 900°C Hold in Air and in N_2

The step in resistance behavior accompanying the environment switch was repeatable, as well as the initial resistance drop. The latter phenomenon might be a

consequence of a convective cooling from the transient high flow rate of the compressed air as the flow meter was readjusted for the switch in gas lines. The step could be the result of the rapid oxidation of the titanium exposed by the hole formation already taken place in the film. Hold test comparisons to the air-annealed samples at 900°C revealed that the nitrogen ambient increased the average lifetime from 44 minutes to 87.5 (figure 3-10).

3.4 Tantalum as an Adhesion Layer

Tantalum films had fewer holes after fabrication than titanium films, as is shown by comparing figure 3-11A to 3-3A. Figure 3-11 also shows that the temperature-induced morphological changes of the tantalum-adhered films were similar to that of the titanium films. The only difference was in the appearance of the sub-micron structures visible in the platinum holes. The Auger analysis results were also similar to those of the Ti/Pt films: oxygen and tantalum were found in the valleys, platinum made up the bulk of the coalesced structures, and there was evidence of silicide formation near the Pt/nitride interface.

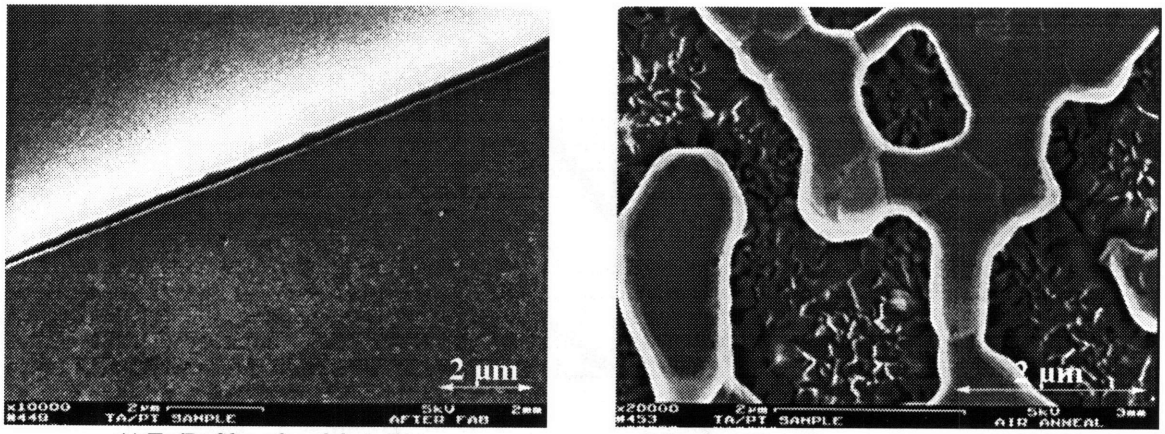

A) Ta/Pt film after fabrication *B)Ta/Pt Film after exposure to 1100°C in air*

Figure 3-11: SEMs of Ta/Pt Samples Before and After Heating

However, the hold measurements revealed that the tantalum-adhered films had a significantly longer lifetime than the titanium-adhered films. The 5% deviation time at 900°C increased from 44 minutes to 220 minutes with the use of tantalum (figure 3-12).

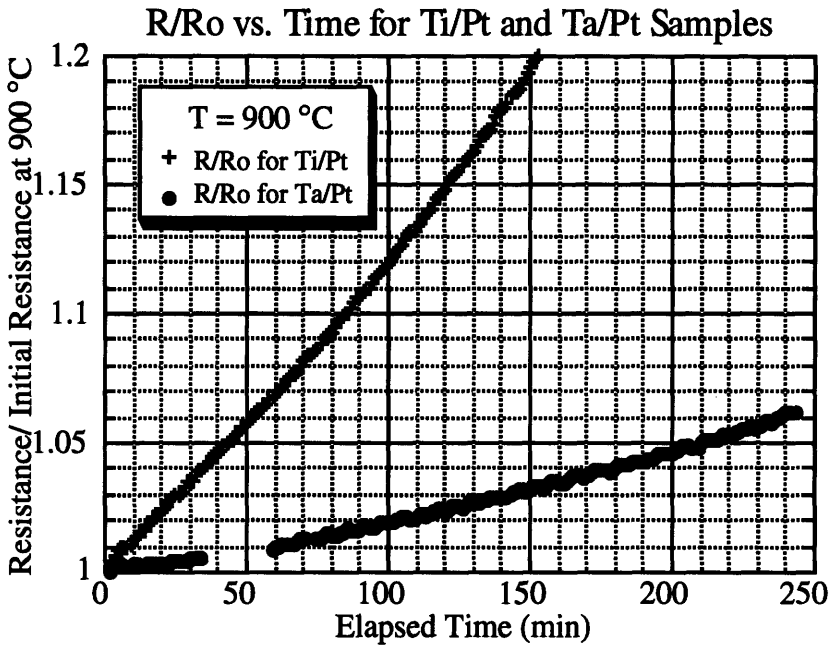

Figure 3-12:Comparison of 900°C Hold for Ta/Pt and Ti/Pt Films

3.5 Behavior with Capping Layers

The lifetime improvement that resulted from annealing in an oxygen-poor environment motivated the fabrication of samples with coatings that would act as an oxidation barrier. Silicon nitride and alumina coatings were both used.

The samples coated with 1000 Å silicon nitride behaved strangely during anneal. The resistance curve, shown in figure 3-13, had four stages. Up until 400°C it behaved like the initial Ti/Pt films, then it changed slope from 400°C until ~520°C, and then changed slope again until ~660°C, where the resistance dropped abruptly. This behavior was repeatable and independent of ambient.

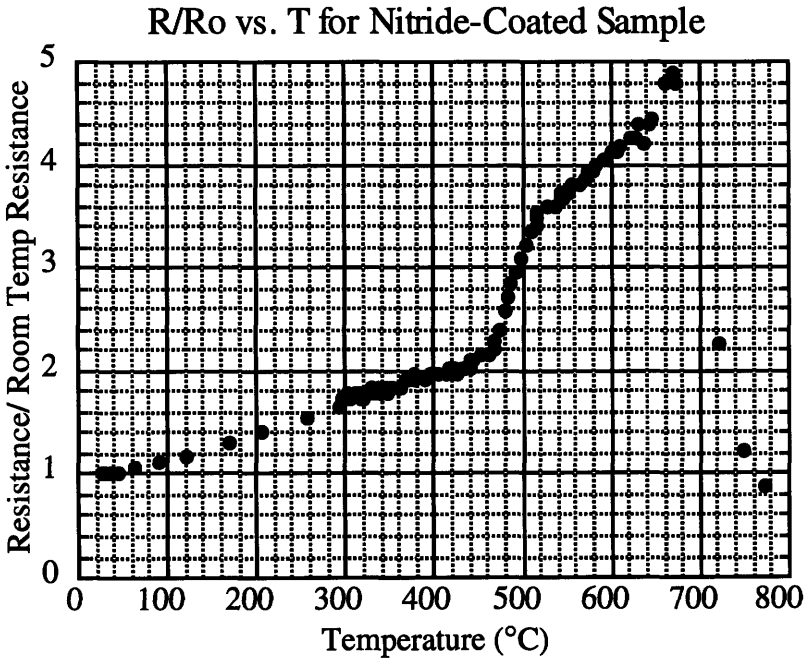

Figure 3-13: Resistance vs. Temperature for Nitride-Coated Sample

The films appeared bubbly in the optical microscope (figure 3-14), and Auger analysis revealed platinum in addition to silicon and nitrogen in the nitride layer. It seems likely that a platinium silicide layer formed during the deposition of the PECVD nitride, and the strange resistance behavior is indicative of that layer growing through diffusion and reaction, and simultaneously experiencing phase change. The nitride is deposited at 300°C, which is the threshold temperature for transforming a platinum film on silicon to PtSi.[37] Examination with the optical microscope also revealed ~100 μm-wide bands of nitride discoloration bordering the metallizations. These bands could be symptomatic of silicide in the nitride regions; the sudden resistance drop at 660 °C could be due to silicide formation shorting the bond pads together.

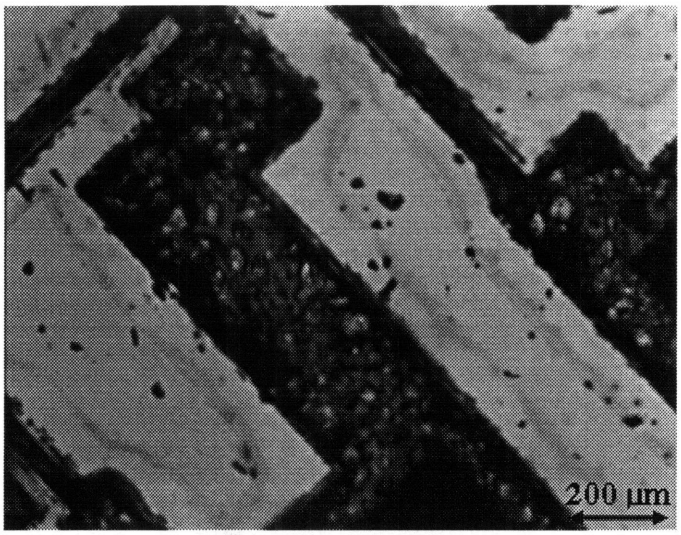

Figure 3-14: Nitride-Coated Films After Exposure to 800°C
(The dark areas are the metallization)

The addition of the 300 nm alumina adhesion layer, however, dramatically improved the behavior of the films, as is shown in figure 3-15. The average lifetime of the Ti/Pt films at 900 °C improved from 44 minutes to 292 minutes with the addition of an alumina layer. Examining the alumina-coated films under the optical microscope after heating (figure 3-16), some hole formation was observed in the alumina. Where the hole had formed, the underlying platinum films had evolved into the islands observed for uncoated-films. The film still covered by alumina, on the other hand, was still relatively intact and in only the initial stages of hole growth.

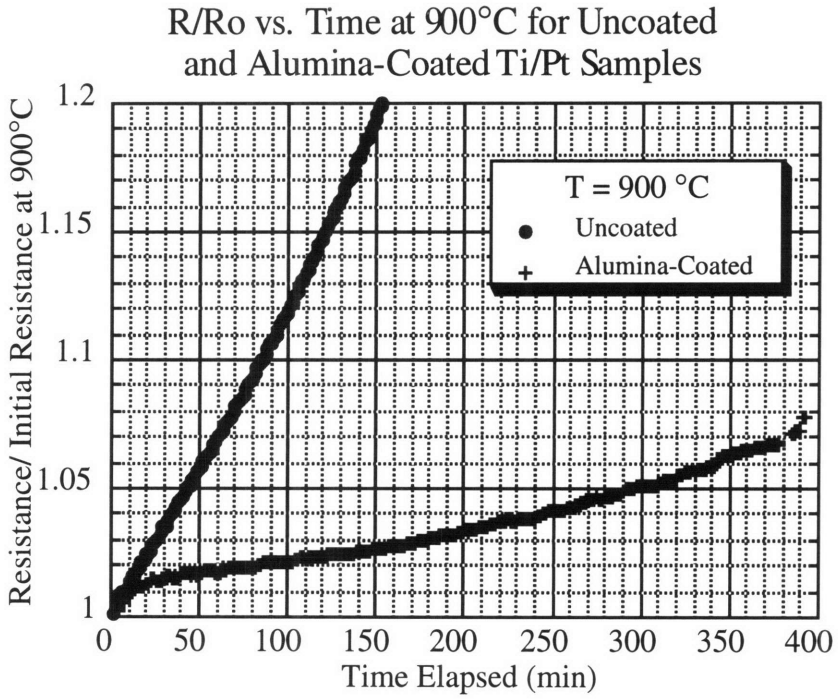

Figure 3-15: Comparision of 900°C Hold for Uncoated and Alumina-Coated Samples

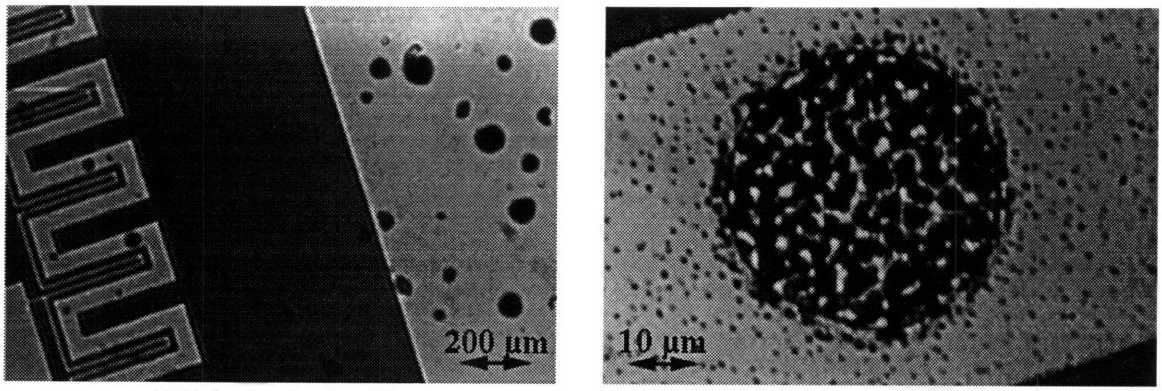

A) Holes in alumina film *B) Close up of hole*

Figure 3-16: Optical Microscope Image of Alumina-Coated Film AfterHeating

3.6 Heat Treatment Effect

An interesting phenomenon was observed with the Ta/Pt films. A sample that had been brought up to 1100 °C in N_2 and held for an hour exhibited the same coalescence phenomena under optical microscope inspection as the other films, but when the same sample was then brought to 1000 °C and back in air, the dependence of resistance on temperature was linear and did not exhibit drift (see figure 3-17). This same phenomenon was subsequently observed in Ti/Pt films, and in films annealed in air instead of nitrogen.

The mechanism for the phenomena therefore appears to be independent of adhesion layer material and ambient.

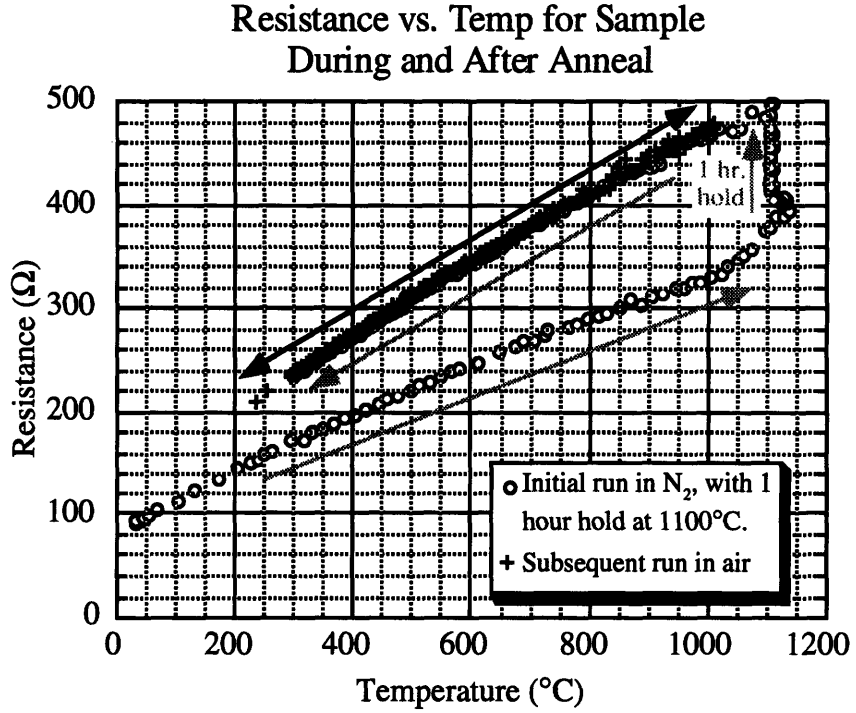

Figure 3-17: Heat Treatment Effect

While this promises a possible solution to the metallization need through the addition of a high temperature anneal to the process, it may not be the ideal solution if the long-term stability of the metallization is poor.

3.7 Thickness Dependence

The dependence of the degradation phenomena was explored with Ta/Pt samples because of the improved lifetime of Ta-adhered films. Three thickness variations were tested, in addition to the standard 10 nm Ta/ 100 nm Pt samples: 20 nm Ta/ 100 nm Pt, 10 nm Ta/ 200 nm Pt, and 10 nm Ta/ 400 nm Pt. Doubling the tantalum thickness drastically reduced the lifetime of the films at 900°C from 220 minutes to 43 minutes. Doubling the platinum thickness increased the lifetime from 220 minutes to 985. The 900 °C lifetime of the 400 nm Pt samples was ~2881 minutes. A summary of the 900 °C lifetimes for all the material combinations is given in table 3.1.

Material	Average Lifetime (min)	No. of Samples	Std. Dev. (min)	Comparison
10 nm Ti/ 100 nm Pt (Ti/Pt)	44	2	1.4	
10 nm Ti/ 100 nm Pt in N_2	87.5	2	3.5	⇑ 2X vs. Ti/Pt
10 nm Ti/ 100 nm Pt/ 300 nm Al_2O_3	292	1	NA	⇑ 6.6X vs. Ti/Pt
10 nm Ta/ 100 nm Pt (Ta/Pt)	220	3	17.3	⇑ 5.0X vs. Ti/Pt
20 nm Ta/ 100 nm Pt	43	1	NA	⇓ 5.1X vs. Ta/Pt
10 nm Ta/ 200 nm Pt	985	2	21.2	⇑ 4.5X vs. Ta/Pt
10 nm Ta/ 400 nm Pt	2881	1	NA	⇑ 13X vs. Ta/Pt

Table 3.1: 900 °C Lifetimes of Different Material Combinations Tested

3.8 Films on Membranes

Ti/Pt films suspended on nitride membranes were also observed. While the membrane films had the same post-anneal morphological appearance as the substrate-supported films, lifetimes were significantly longer for membrane metallizations: 125 minutes rather than an average lifetime of 44 minutes at 900°C (figure 3-18).

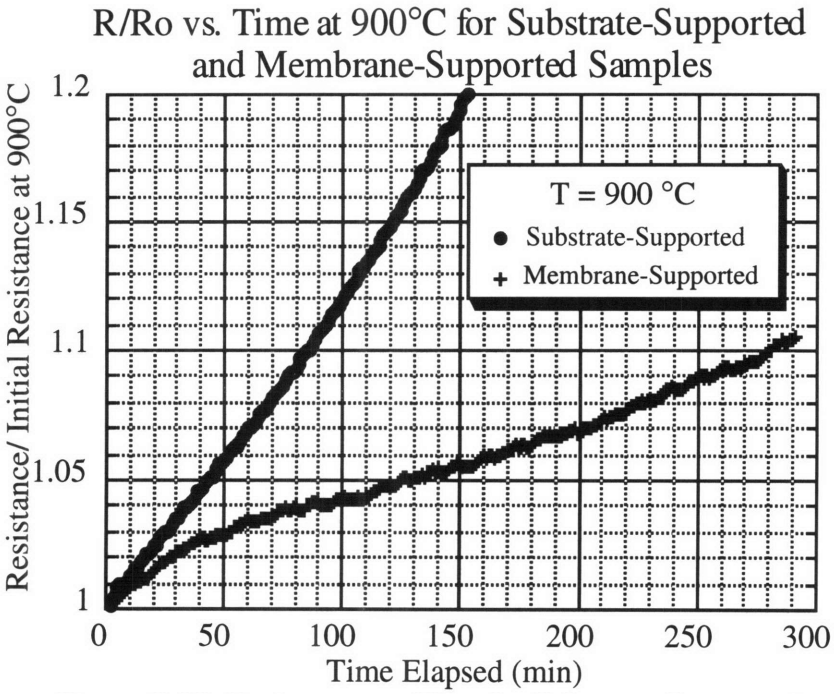

Figure 3-18: Resistance vs. Time for Substrate-Supported and Membrane Samples

Qualitative observations were also made of the membrane fracture. Unpatterned, metallized membranes survived being brought up to 1100 °C in air at 5 deg/minute followed by a one hour anneal at 1100°C. Patterned membranes, however, fractured at ~950 °C as the temperature was being increased at 5 deg/minute in air. Optical microscope observations (figure 3-19) of the fractured membrane indicate that fractures might initiate where the bond pads overhang the membrane and create points of stress concentration.

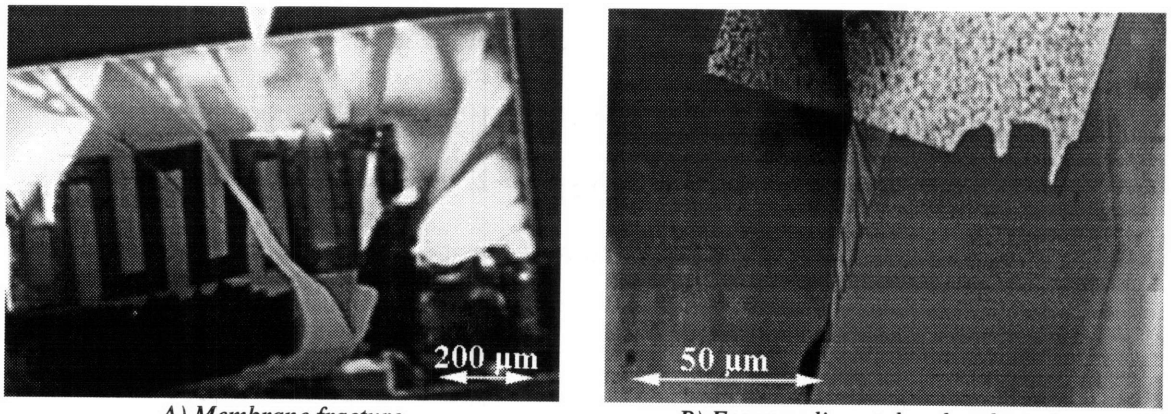

A) Membrane fracture *B) Fracture line at bond pad overlap*

Figure 3-19: Optical Microscope Images of Failure in Uniformly-Heated Membranes

The uniform-temperature resistance measurements, made in the furnace, all used low currents (~1 mA) for sensing the resistance. When large currents are used in the membrane-isolated metallizations, the metal films act as heaters. This is demonstrated by the IV curve in figure 3-20 for a resistor on a membrane. The sample was not heated in the furnace, so that far from the membrane the sample was at room temperature.

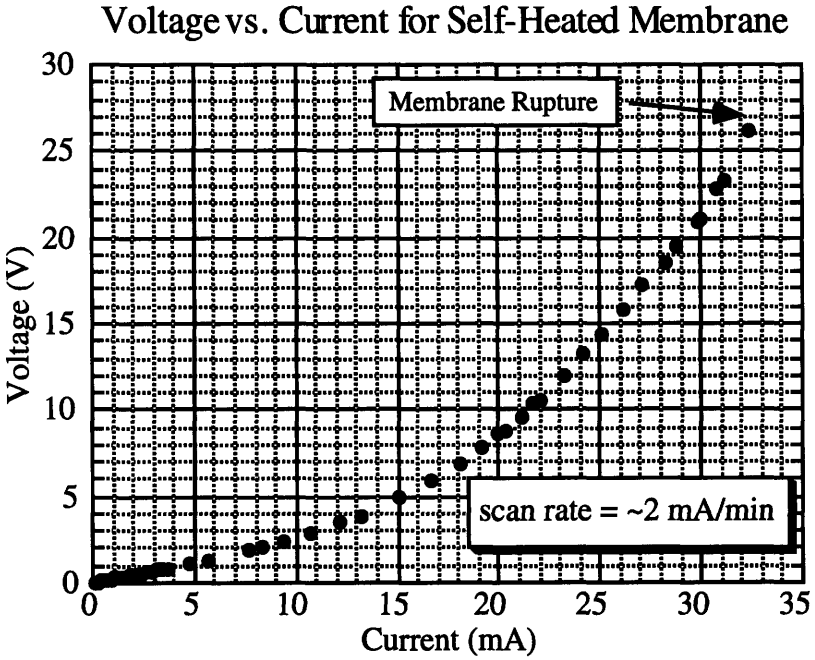

Figure 3-20: Voltage vs. Current for Membrane Metallization

Using the resistance dependence on temperature found in the uniformly-heated films, the IV characteristic can be translated into a temperature-power relationship for the heater (figure 3-21). The temperature is the average over the whole resistor. There is significant spatial nonuniformity in the temperature profile, which is reflected in the appearance of the metal films after heating (figure 3-22). Electromigration might also play a role in degradation because of the higher current density (~7000 A/cm^2 at fracture).

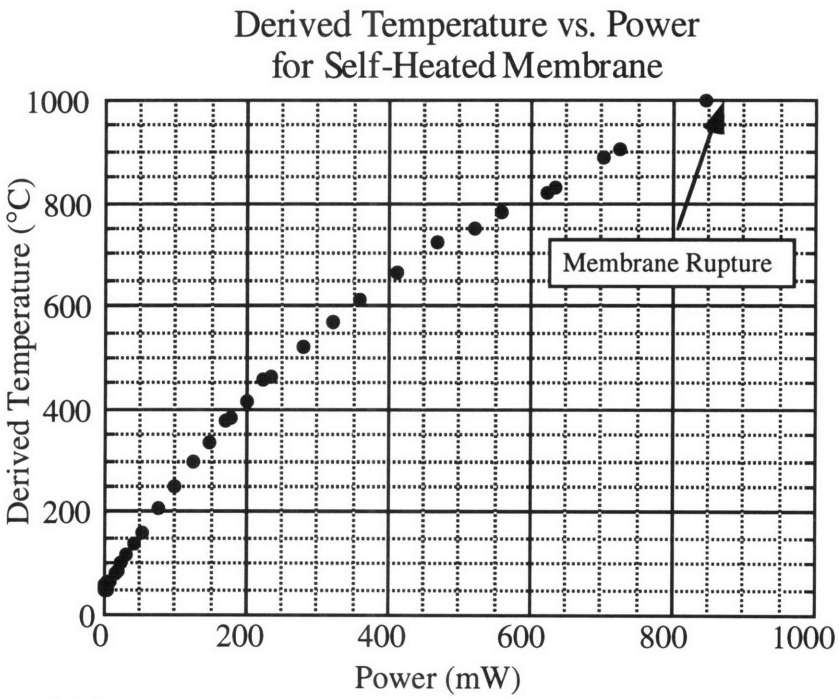

Figure 3-21: Derived Temperature vs. Power for Membrane Metallization

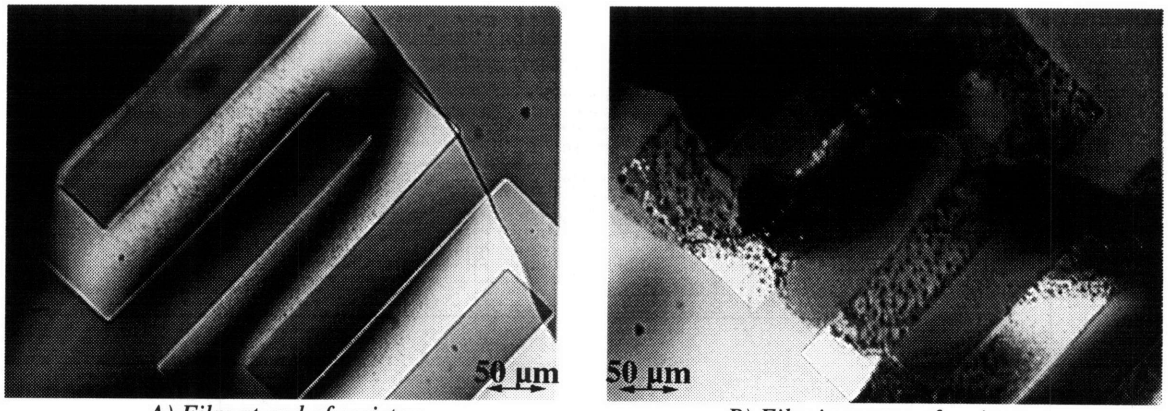

A) Film at end of resistor *B) Film in center of resistor*

Figure 3-22: Degradation in Resistor Metallizations After Self-Heating

For this sample, the temperature at a given power was almost twice that as was observed in the microreactor heaters[6]. The difference is probably due to the absence of the platinum catalyst on the reverse side of the membrane, which roughly doubles the heat transfer away from the resistors. The average temperature of the resistor just before fracture was ~1000 °C. The uniformly-heated membranes, on the other hand, fractured at 950°C. The increase in fracture temperature is probably due to the localization of the heat to the center of the membrane, where stress can be relieved by deformation.

3.9 Stress Measurements

Wafer curvature measurements were made on three wafers: one coated only with the 1 μm of nitride (figure 3-23), one with 1 μm nitride/ 10 nm Ta/ 100 nm Pt (figure 3-24), and one with 1μm nitride/ 10 nm Ti/ 100 nm Pt (figure 3-25). Each wafer was brought up to 900 °C at 10 °/min, and the curvature measured every two minutes. The temperature was held at 900 °C for 20 minutes before returning to room temperature at about 10 °/min (below ~400 °C, the machine cooled more slowly).

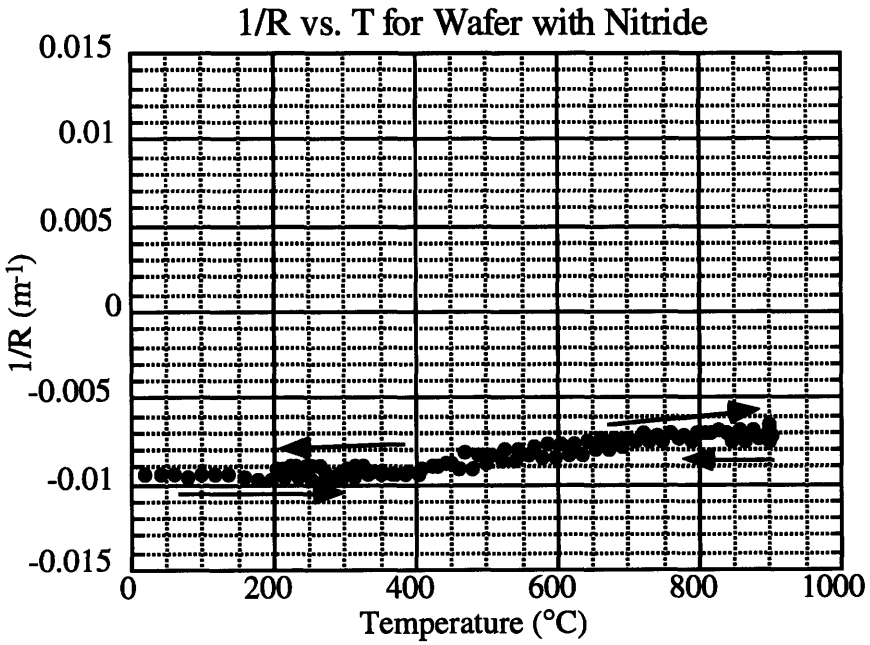

Figure 3-23: Inverse Radius of Curvature vs. Temperature for Nitride-Coated Wafer

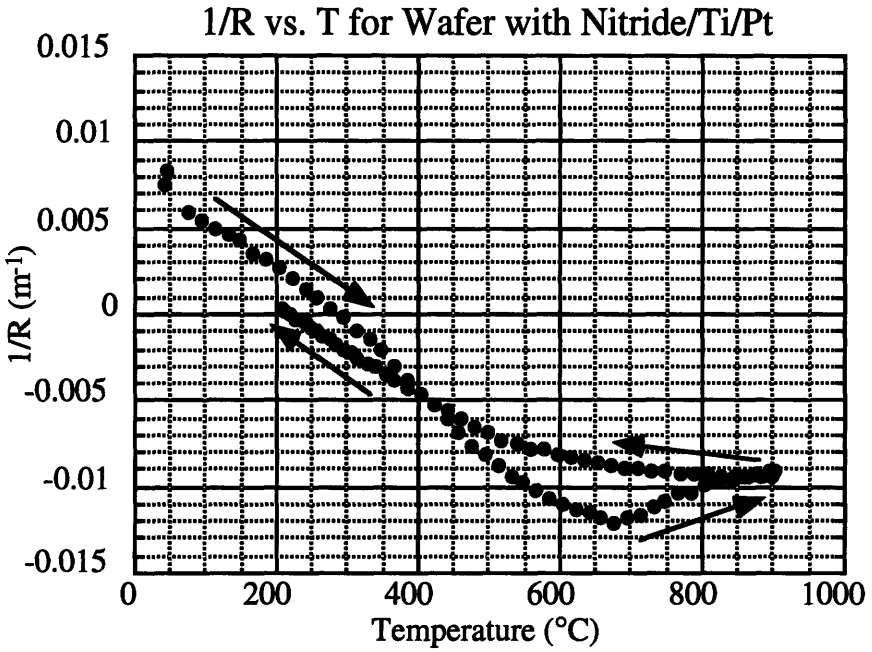

Figure 3-24: Inverse Radius of Curvature vs. Temperature for Nitride/Ti/Pt Wafer

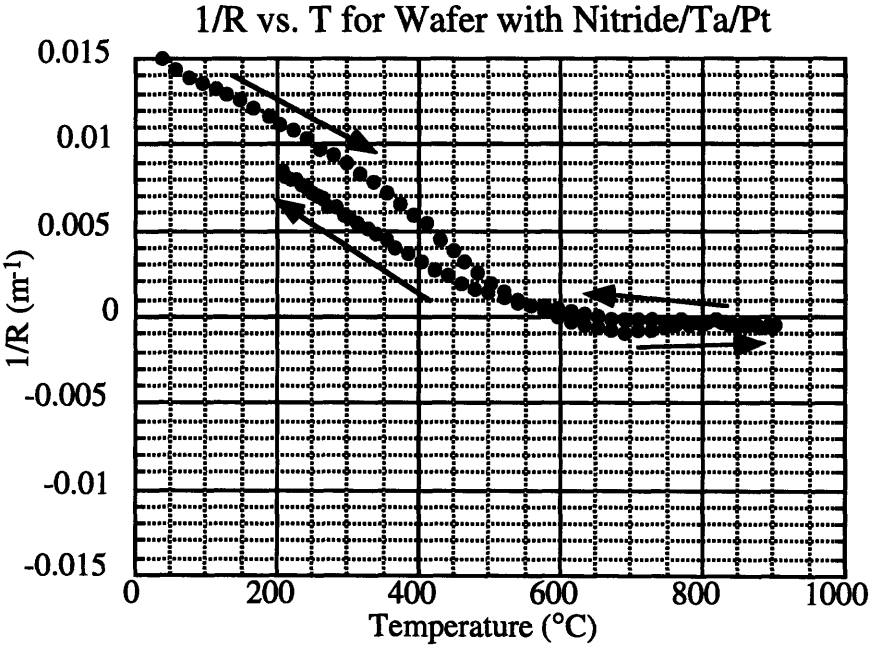

Figure 3-25: Inverse Radius of Curvature vs. Temperature for Nitride/Ta/Pt Wafer

The curvature of all the samples remained constant during the twenty-minute hold at 900 °C. The stress was calculated using equation (1) on page 25, assuming that the plain nitride wafer had the same curvature as the nitride wafers underlying the metal films in the

other wafers. The estimated stresses (figures 3-26 and 3-27) are a little higher than expected, indicating that our assumption of the underlying nitride-coated wafers having the same curvature may be incorrect. It is clear, however, that the films are tensile as deposited. This is to be expected because the wafers in the evaporator were probably well above room temperature when the platinum was deposited. The films become less tensile with increasing temperature, which we expect from the thermal expansion mismatch between the films and the niride. The films are less tensile after the thermal cycle, indicating that some stress relaxation did take place, only it was relaxation not of the compressive stress induced by heating, but relaxation of the tensile stress incurred in deposition. The Ti/Pt plot has a local minimum at ~675°C, while the Ta/Pt plot does not. This could be due to the Ti/Pt sample reaching the compressive yield point of the platinum. The Ta/Pt film, on the other hand, never becomes compressive, and so the yield is not achieved.

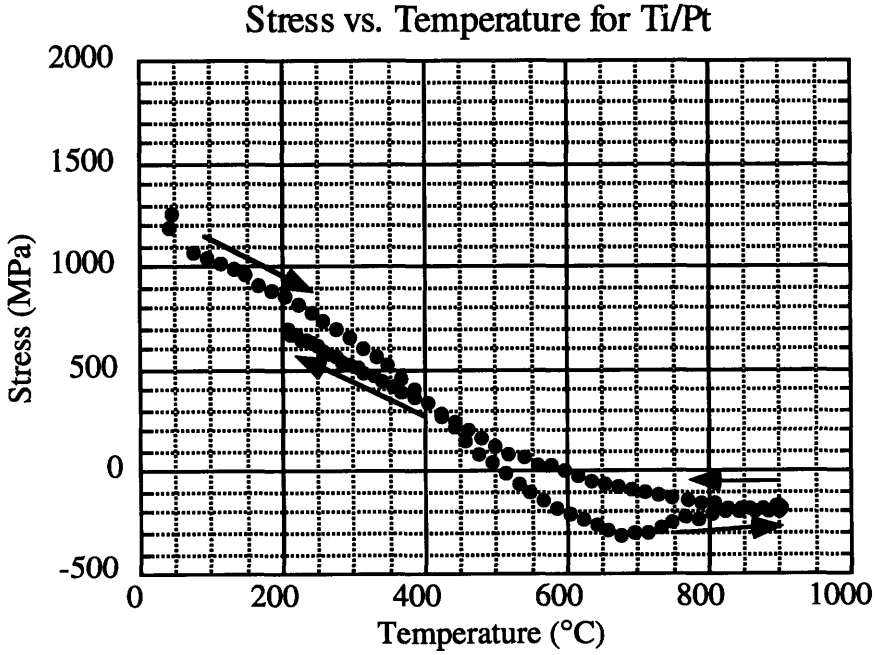

Figure 3-26: Estimate of Stress vs. Temperature for Ti/Pt Film

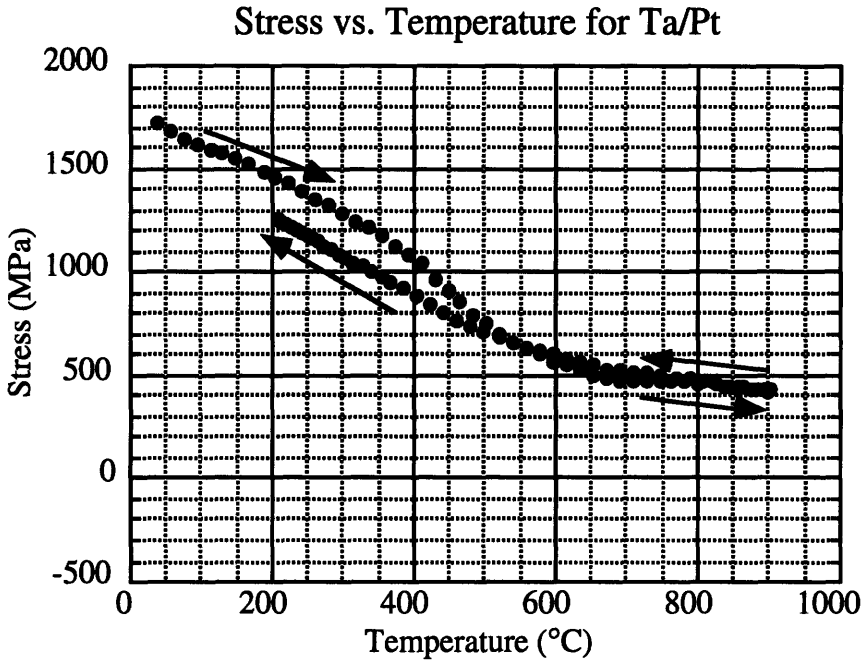

Figure 3-27: Estimate of Stress vs. Temperature for Ta/Pt Film

Chapter 4

Discussion

To summarize the data: degradation is retarded by oxygen-poor ambients, thicker Pt films, alumina coating layers, suspension on a membrane, and the use of Ta as an adhesion layer instead of Ti. Degradation is accelerated by thicker adhesion layers and higher temperatures. SEMs of the films show that the film is forming holes which are growing over time. AES indicates oxidation of the adhesion layer and silicide formation near the interface for both the Ta- and Ti-adhered films. Clearly, many degradation mechanisms are at work. In order to understand and prevent metallization degradation, we need to determine which events are dominant or rate-limiting. But first, we need to determine the relationship between the resistance change and morphology.

4.1 Relating Resistance to Morphology

Constant volume, the observation of which is discussed in section 3.1, is assumed in relating resistance to hole formation in the films. The resistance of the film should change with hole formation, because the holes distort the electric field lines in the conductor, forcing the electrons to traverse a more circuitous path. Much work has been done on the modeling of transport in heterogeneous materials as they change composition. This can be applied to the platinum films studied here if one considers the holes in the film to be cylinders of some other media with a negligible conductivity. Most of these studies have focused on the point in composition at which transport begins to occur, called the

"percolation threshold." In particular, Kirkpatrick[38] numerically modeled the conduction in a heterogeneous media as a resistor network based on lattice models. Ahmad and Evans[39] applied this solution method to modeling resistance near the percolation threshold for conductivity in sputtered platinum films, and were able to match their model with experimental data.

A simpler model, developed by Bruggeman[40] in 1935, which considers spheres of one conductivity suspended in a material of another conductivity, can be used to develop insight far from the percolation threshold limit. McLauchlan[41] simplifies Bruggeman's equation for the 2D case where circles of zero conductivity are interspersed in a sheet of σ_o conductivity as,

$$\sigma_m = (1 - f)^2 \sigma_o \qquad (2)$$

where f is the fraction of total circle area over total film area. The 2D case is more applicable to the degraded platinum films than the 3D case, because the holes are closer in shape to cylinders than spheres. Figure 4-1 compares this model to data obtained from comparing resistance measurments to SEM pictures. The model appears to be reasonable, particularly considering the large error margin in estimating average hole size and separation from SEM photos. The data has resistances that are a little higher than what is predicted by the model, which should be expected because the the surfaces and structures of the actual films are more disordered than the perfect cylinders and flat films of the model, which further increases the resistance to electron transport.

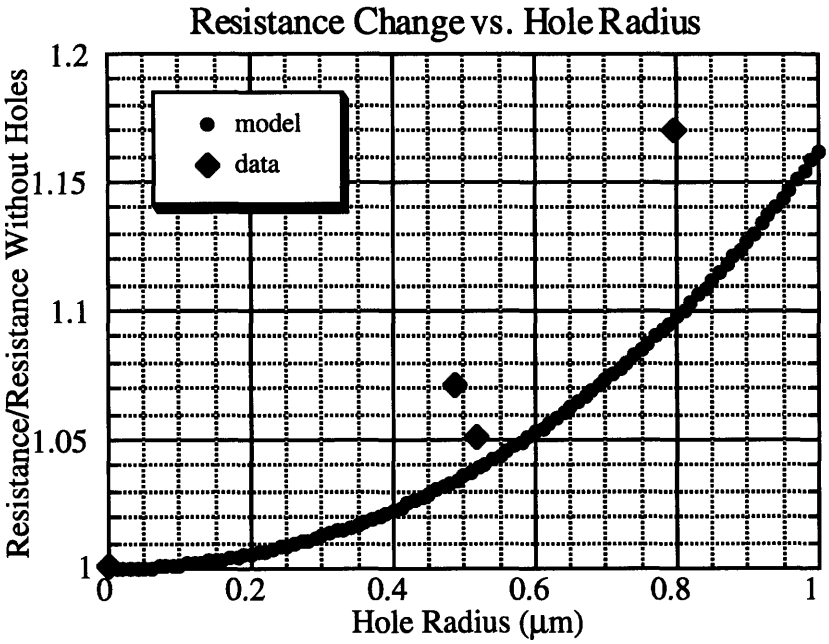

Figure 4-1: Relation of Hole Radius to Resistance

The model and data clearly show that the observed morphological change is related to the resistance increase. The source of the morphological variation is now examined.

4.2 Oxygen Diffusion and Interlayer Reaction

The nitrogen/air studies and the composition analyses indicate that oxygen plays a role in the degradation. However, oxygen diffusion through the platinum does not appear to be the rate-limiting step. Several things support this assertion. For one thing, the degradation still took place in a nitrogen ambient and with the alumina capping layer. The oxygen incorporated into the adhesion layer during fabrication should already have fully interacted with the Ti film before reaching high temperatures and would not be the cause of a delayed reaction. However, pinholes in the alumina film or oxygen outgassing in the furnace during nitrogen runs could also explain this data and still be consistent with an oxygen-diffusion limited model. The large reduction in lifetime that resulted from doubling the adhesion layer thickness is not consistent with such a model. If the degradation was limited by the diffusion of oxygen through the platinum, changing the thickness of the adhesion layer would have no effect on the lifetime.

In addition to the evidence of oxidation, the chemical analysis also reveals silicide formation near the nitride/platinum interface. It is unlikely that either of these reactions would be rate limiting for the degradation, since both readily occur when the respective elements are brought into contact at the temperatures studied here. Also, neither of these chemical reactions would explain the dramatic changes in morphology observed. The formation of some eutectic might explain the transformation, but while the Ti-Pt system has a eutectic temperature in the range examined, the Ta-Pt system does not. Yet the degradation of the two different metallizations is very similar, indicating that the same fundamental mechanism is at work.

Furthermore, the chemical analysis did not reveal any of the observations of Ti-Pt reaction or TiO_2 encapsulation of Pt as were observed by other groups. This might simply be because the metallizations in this work had a much higher Pt:Ti ratio. The Ti would preferentially react with oxygen over the platinum, and therefore all of the titanium layer was oxidized before it could react with the platinum.

4.3 The Role of Stress

The increased lifetime of the membrane-supported films compared to the substrate-supported films indicates that stress may be involved in the degradation of the films. The only difference between the membrane-support and the substrate-support that the film "sees" is that on the membrane, some of the stress in the film can be relieved through deflection. The wafer curvature measurements indicate that the films are highly tensile, and that the tensile stress is reduced after a thermal cycle. This relaxation does not take place at 900 °C, however, where the radius of curvature remained constant throughout a 20 minute hold. The relaxation probably takes place at mid-range temperatures, where the atomic mobility is sufficient for relaxation while the tensile stress is still large. This is not consistent with stress relaxation motivating the morphological changes, which we know

from our resistance measurements to occur during 900°C holds. It is, however, possible that the tensile stress contributes to hole formation, which is preliminary to the growth of the holes and subsequent resistance change.

4.4 Agglomeration

The data is consistent with hole formation and agglomeration. Surface diffusion, which is the mechanism by which agglomeration occurs, is rapid for platinum in the temperature range of interest (the diffusivity of the (001) platinum surface is ~1.0×10^{-5} cm^2/s at 900°C)[42]. From SEM images it is clear that significant grain grooving is occuring, which could result in hole formation. In fact, Srolovitz and Safran[43] predict that the thermodynamic equilibrium for the groove depth d of a film, with a grain size 2R and an equilibrium notch angle Φ, is given by:

$$d = R \frac{2 - 3\cos\Phi + \cos^2\Phi}{3\sin^2\Phi} \qquad (3)$$

Assuming a grain size of 2 μm, which is about the largest size observed in the SEMs, and the worst case notch angle of 90°, the equilibrium groove depth could be as large as 667 nm. Also, equation (3) is derived for the intersection of two grains; where three grains intersect groove depths are larger. The minimum radius hole required for hole growth to be thermodynamically favored[26] is given by,

$$R_C = \frac{h}{1 - \cos\alpha} \qquad (4)$$

where α is the wetting angle of the platinum on the adhesion layer and h is the film thickness. For two materials that are completely adhesion-adverse, the critical radius would be half the film thickness, or 50 nm in the case of the 100 nm films. In the films examined here, the holes already present after fabrication as observed in the SEMs (see figure 3-3) have a radius ~50 nm.

The dramatic increase in lifetime that resulted from the alumina capping model is consistent with agglomeration, since the alumina would constrain the top surface of the platinum layer. The observations of oxygen diffusion enhancing degradation are also consistent with agglomeration, as the oxygen at the Ti-Pt and Ta-Pt interface would reduce the adhesion of the platinum layer. The increased lifetime of Ta/Pt films compared to Ti/Pt films might be because of titanium's greater affinity for oxygen or because there are fewer holes in the Ta/Pt films than in the Ti/Pt films after deposition. This difference in pinhole density could in turn be a consequence of differences in oxygen affinity, or a difference in the deposition conditions. A thicker adhesion layer would increase the amount of oxygen at the interface, and hasten agglomeration. Doubling the platinum thickness resulted in a 4.5-fold increase in lifetime, and quadrupling the platinum thickness resulted in a 13-fold lifetime increase. The trend is consistent with Jiran and Thompson's observation that the hole growth rate is a strong function of temperature, but they predict an inverse cubic dependence.[44] This data, however, reflects both hole formation and hole growth. If the hole formation rate is comparable to that of hole growth, both mechanisms must be considered in order to quantitatively analyze the thickness dependence of the phenomena.

The observation of increased resistance stability after a high temperature anneal, independent of adhesion layer material or anneal ambient, is also consistent with agglomeration. The high temperature anneal drives the sample closer to equilibrium, reducing the driving force for agglomeration in subsequent processing at lower temperatures. Even after the heat treatment, the system is not yet stable, and will agglomerate at lower temperatures given enough time.

Assuming a resistance/radius dependence given by (2) and a hole density of ~14 holes/ 100 sq. μm, estimated from SEM photos, we can interpret the data shown in figure 3-6 as the average hole radius in a film as a function of temperature, shown below in figure

4-2. From this interpretation, which includes both hole formation and growth stages, the hole radius appears to first grow as $t^{1/2}$, and then to grow linearly. This is consistent with models of agglomeration developed for single-layer films, even though this film has two layers which are both reacting and agglomerating.

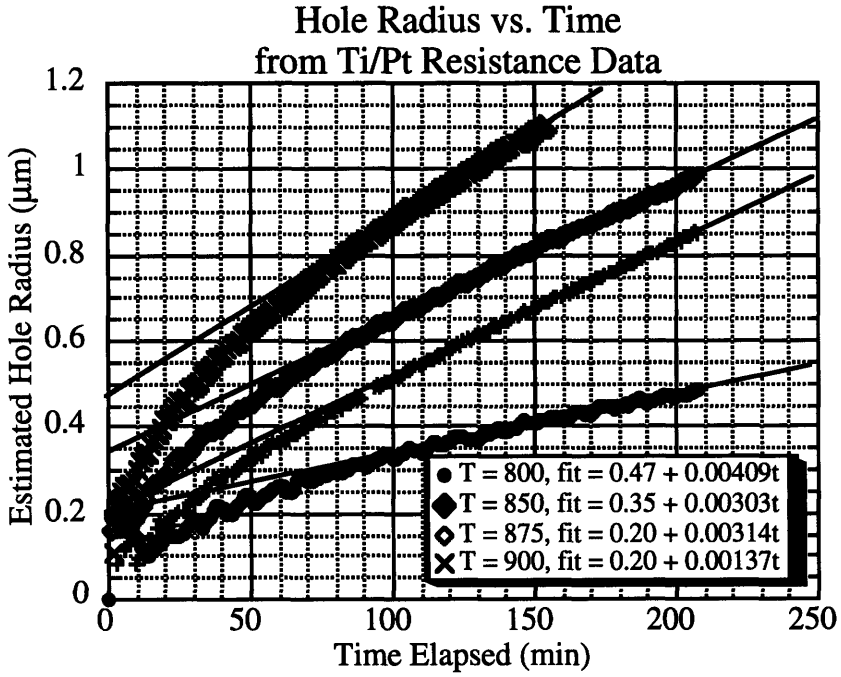

Figure 4-2: Hole Radius as a Function of Time Interpreted from Ti/Pt Hold Data

Srolovitz[26] predicted that the hole radius will initially grow as $\sim t^{1/4}$ and then be linear with time, and that a stressed film would grow initially as $\sim t^{1/3}$. Jiran and Thompson isolated hole formation from hole growth in their work, and they predicted that the hole growth rate should be constant. The equation Jiran and Thompson derived for hole growth rate is as follows[44]:

$$\frac{dr}{dt} = \beta \frac{\exp(-Q_s/kT)}{kTh^3} \qquad (5)$$

where β is a constant that is proportional to the surface tension and the square of the atomic volume, Q_s is the activation energy of the surface diffusivity, T is the temperature, h is the film thickness and k is the Boltzman constant.

Published values for the activation energy of self-diffusion on platinum surfaces range from 0.47 eV[42] to 0.63 eV[45]. Fitting lines to the radius growth estimate data and assuming the temperature dependence given in (5), the activation energy is approximated as 1.239 eV (figure 4-3). Given the large error margin, this is reasonably consistent with platinum surface diffusion.

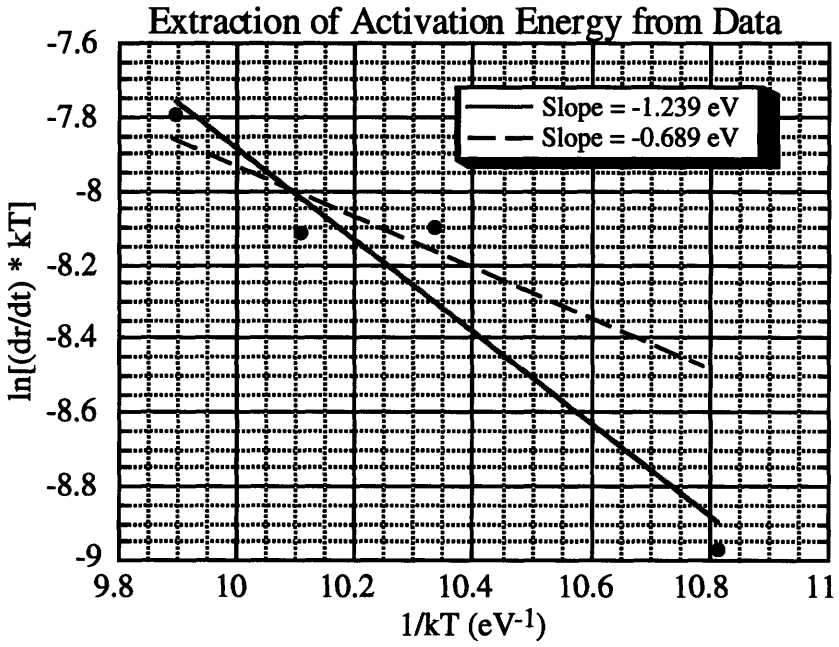

Figure 4-3: Extraction of Surface Diffusion Activation Energy from Data

As was discussed in section 4.2, stress is clearly playing a role in the degradation, most likely in hole formation. However, from this work it is yet unclear what role stress might play in hole growth. Resistance measurements that compare membrane-supported and substrate-supported films might be an excellent means of quantifying the dependence of agglomeration on stress, particularly if a new mask set was made with large membranes and straight-line patterns. Aluminum could be used instead of the double-layer film to eliminate the complications of interlayer interractions. Patterns with intentional holes could be used to isolate the effect of stress on hole nucleation and hole growth separately. This interesting tangent is not explored in this thesis, however.

4.4 The Complete Degradation Picture

The complete hypothesis for the degradation mechanism, illustrated in figure 4-4, has two stages. In the first stage grain grooving occurs in both the platinum and titanium/tantalum layers, while at the same time oxygen is diffusing through to the adhesion layer and reacting. Tensile stress might also assist in hole formation. In the second stage, once holes of the critical radius for agglomeration form in the platinum film, the platinum begins to pull away from the oxide that has formed beneath it. Meanwhile, the oxidizing adhesion layer has formed holes of its own as the titanium migrates towards the areas of higher oxygen concentration. Where the platinum comes into contact with the silicon-rich nitride, it reacts to form a silicide, and this increases the adhesion of the platinum to the vacancies in the oxide. Eventually, the film will be completely segregated, with titanium (or tantalum) oxide in some areas and platinum-platinum silicide in others.

By creating areas of stronger adhesion, the platinum silicide formation may in fact retard agglomeration. This provides another explanation for the decreased lifetime that resulted from doubling the thickness of the tantalum layer. In that case, holes grew less readily in the adhesion layer, giving the platinum less access to the nitride beneath, and therefore reducing the number of areas where the platinum layer could be "pinned" to the nitride layer by silicide formation.

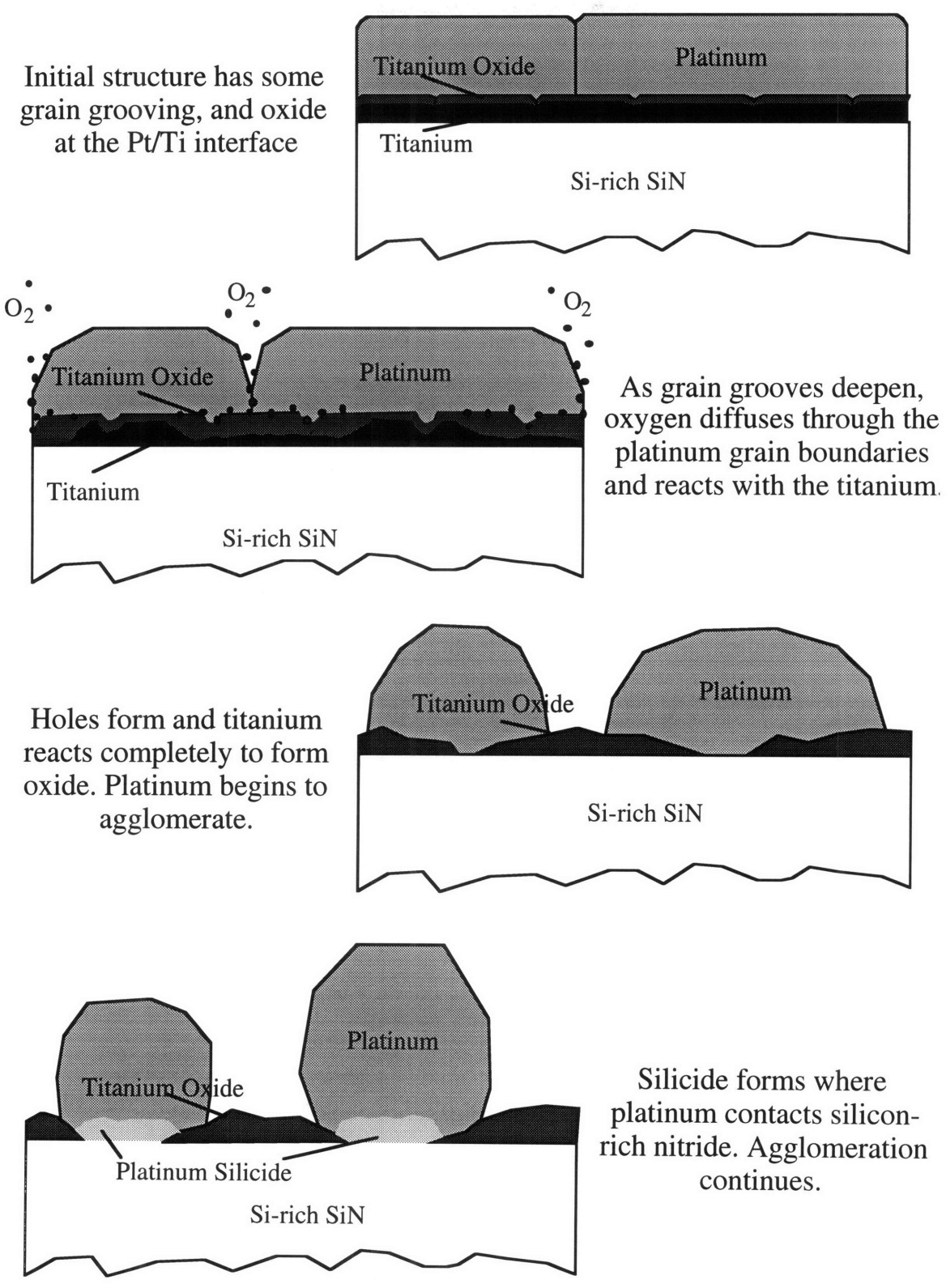

Figure 4-4: Illustration of Hypothesized Degradation Process

Chapter 5

Conclusions

Agglomeration dominates the degradation of the thin films used in the microreactor. Oxygen enhances the degradation by reacting with the titanium and tantalum layers and consequently reducing their adhesion with the platinum. Improvements were observed with the use of alumina coating layers, tantalum adhesion layers and thicker films. These results suggest several possible solutions for the microreactor metallization degradation problem.

The heat treatment approach, suggested by the observations discussed in section 3.6, is probably not the best solution, because the final resistance/temperature curve would be highly dependent on the processing conditions. As a result, the sensors and heaters would have to be calibrated for each new microreactor. Also, since the system has already begun to agglomerate, the long-term stability would not be as good as for a system where agglomeration was altogether avoided.

The simplest solution is to use thicker films. In addition to decreasing the hole growth rate, thicker films also increase the size required for the initial hole to be thermodynamically favored to grow, as well as the depth of groove required to form the hole. Using equation (3) and assuming a grain size of 2 μm, we estimated the worst case minimum thickness for which thermodynamics does not predict hole formation through grain grooving to be ~667 nm. Future generations of the microreactor may want to use

metal layers as thick as 1 μm. An additional advantage of the thicker film solution, in the case of the microreactor, is that it can also increase the stability of the platinum catalyst metallization.

Thicker films would, however, stress the membranes more during thermal cycling. The use of a single-crystal silicon membrane instead of a nitride membrane would make the membranes more robust, as would arranging the metallization pattern on the membrane so as not to create points of high stress. If the heater and sensor metallization were to mirror the catalyst metallization, for example, the stress would be balanced out. Also, the membrane could have structures designed to deform readily in order to reduce stress in the critical regions---a sort of micro shock absorber.

A coating layer would also increase the lifetime of the films by interfering with surface diffusion, and hence retarding both hole formation and hole growth. An oxygen diffusion barrier material such as alumina would also slow the oxidation of the adhesion layer. The seven-fold increase in lifetime for the alumina-coated films supports this hypothesis. In addition, a uniform coating over the entire reactor would strengthen the reactor membrane without increasing the separation between the heaters and sensors, and the catalyst.

Another way to reduce agglomeration might be to alloy the platinum with some other metal. This method is often used to retard atomic diffusion in order to reduce electromigration. The presence of trace amounts of copper and silicon in aluminum films, for example, has been observed to increase the mean time to failure due to electromigration nearly 100 times.[46] Also, other refractory metals might be considered instead of platinum. As a rule of thumb, the surface diffusivity at a given temperature will be smaller for a material with a higher melting point. Irridium, for example, melts at 2407°C. Tungsten has

a high melting temperature, but it oxidizes readily, and therefore would not make a good metallization in this case.

Improving the adhesion of the metallization is another possible solution. Silicides, for example, would adhere readily to the silicon-rich nitride. Platinum silicide is not a potential candidate, because it has been observed to be unstable at temperatures above 600°C.[47] Many silicides, such as PtSi, $CoSi_2$, WSi_2, and $MoSi_2$ are unstable in high temperature oxidizing atmospheres when supported on SiO_2. $TiSi_2$, however, is known to be stable in high-temperature oxidizing ambients both when supported on SiO_2 and when supported on Si. $TaSi_2$ is known to be stable up to 1000°C.[48] Silicides are made by sintering a thin-film metal-silicon composite. The composite can be formed through a variety a methods, but the most reliable for controlling silicide composition is cosputtering metal and silicon.[48] The use of silicides would complicate the current microreactor fabrication process, but might be a solution if the other measures are insufficient.

In conclusion, this work combined chemical analysis, microscopy, and a novel in situ resistance measurement technique to examine the high-temperature behavior of the titanium-adhered platinum films used for heating and temperature sensing in a silicon-based microfabricated chemical reactor system. Many mechanisms appear to play a role in the degradation of thin platinum films, including stress and interlayer reaction, but the dominant mechanism is agglomeration, a surface-diffusion-driven capillarity process. Tests with alumina-coated samples, and double- and quadruple-thickness samples demonstrate that the lifetime of the metallizations can be increased by making the platinum thicker and by adding coating layers, which is consistent with an agglomeration degradation mechanism. It is predicted that films as thick as 1 μm will not undergo agglomeration, and might therefore increase the temperature range of operation of the silicon-based chemical reactor cell.

Appendix A

Sample Fabrication

The following is a detailed process flow for sample fabrication. Many variations of wafers were manufactured for testing: samples with patterned metal layers on substrate-supported nitride, samples with patterned metal layers and coating layers on substrate-supported nitride, samples with patterned metal layers on membranes, and samples with unpatterned metal layers on membranes. All of the samples began as lightly p-doped, double-polished <100> silicon wafers. The process is written as if for samples that combine patterned metal layers with membranes and coating layers. Different simplifications of this process are then used to produce each of the sample combinations. In order to reduce complexity, the steps have been divided into blocks. The fabrication blocks for the different types of samples are as follows:

Substrate-Supported Patterned Metal Layers
- I. Wafer Clean and Nitride Deposition (steps 1-3)
- II. Pre-Patterning of Metal Layer (steps 18-26)
- III. Deposition of Metal Layer (steps 27-32)
- IV. Dicing Up Samples (steps 43-45)

Membrane-Supported Patterned Metal Layers
- I. Wafer Clean and Nitride Deposition (steps 1-3)
- II. Patterning Backside Nitride for KOH Mask (steps 4-17)
- III. Pre-Patterning of Metal Layer (steps 18-26)
- IV. Deposition of Metal Layer (steps 27-32)
- V. Membrane Release (steps 33-34)
- IV. Dicing Up Samples (steps 43-45)

Membrane-Supported Unpatterned Metal Layers
- I. Wafer Clean and Nitride Deposition (steps 1-3)
- II. Patterning Backside Nitride for KOH Mask (steps 4-17)
- III. Deposition of Metal Layer (steps 27-28, 31-32)
- IV. Membrane Release (steps 33-34)
- V. Dicing Up Samples (steps 43-45)

Substrate-Supported Patterned Metal Layers with Nitride Coating Layer
- I. Wafer Clean and Nitride Deposition (steps 1-3)
- II. Pre-Patterning of Metal Layer (steps 18-26)
- III. Deposition of Metal Layer (steps 27-32)
- IV. Deposition and Patterning of Nitride Passivation Layer (steps 35-42)
- IV. Dicing Up Samples (steps 43-45)

Substrate-Supported Patterned Metal Layers with Alumina Coating Layer
- I. Wafer Clean and Nitride Deposition (steps 1-3)
- II. Pre-Patterning of Metal Layer (steps 18-26)
- III. Deposition of Metal Layer (steps 27-32)
- IV. Dicing Up Samples (steps 43-45)
- V. Deposition and Patterning of Alumina Passivating Layer (steps 46-55)

STEP	STEP DESCRIPTION	FACILITY
	Wafer Clean and Nitride Deposition (All Wafers)	
1	RCA wafer clean	RCA station (ICL)
2	deposit 1 μm silicon-rich nitride on front and back	VTR Tube (ICL)
3	RCA wafer clean right before patterning	RCA station (ICL)
	Patterning Backside Nitride for KOH Mask (Membrane Wafers Only)	
4	HMDS deposition	HMDS oven (TRL)
5	coat front of wafer with 1 μm OCG 825 (resist: 6 s. at 500 rpm; spread: 6 s. at 750 rpm; spin: 30 s. at 3500 rpm)	coater (TRL)
6	prebake 5 min. at 90°C	prebake oven (TRL)
7	coat back of wafer with 1 μm OCG 825 resist	coater (TRL)

8	prebake 5 min. at 90°C	prebake oven (TRL)
9	coat back of wafer with 1 μm OCG 825 resist	coater (TRL)
10	prebake 20 min. at 90°C	prebake oven (TRL)
11	exposure of backside with nitride mask (figure B1)	Karl Suss[49] 1 Aligner (TRL)
12	develop in OCG 934 1:1 developer (~90 sec)	solvents wet bench (TRL)
13	postbake 30 min. at 120°C	postbake oven (TRL)
14	etch away backside nitride	plasma etcher 1 (ICL)
15	remove photoresist with pirahna clean	acid hood (TRL)
16	dump rinse	acid hood (TRL)
17	spin dry	spin dryer (TRL)

Pre-Patterning of Metal Layer (All Patterned Wafers)

18	HMDS deposition	HMDS oven (TRL)
19	coat front of wafer with 1.38 μm AZ 5214-E (resist: 8 s. at 500 rpm; spread: 8 s. at 750 rpm; spin: 30 s. at 4000 rpm)	coater (TRL)
20	prebake 30 min. at 90°C	prebake oven (TRL)
21	exposure with metal mask (figure B-2) (IR alignment to nitride pattern for membrane wafers)	Karl Suss aligner 1 (TRL)
22	90 sec. bake on plate at 120°C	postbake oven (TRL)
23	flood exposure for 60 sec.	Karl Suss aligner 1 (TRL)
24	develop in AZ 422 MIF (~90 sec)	solvents wet bench (TRL)
25	rinse in DI water	solvents wet bench (TRL)

26	spin dryer: 140 sec. rinse + 240 sec. dry	spin dryer (TRL)
	Deposition of Metal Layer (All Wafers)	
27	descum for ~2 min.	photoresist asher (ICL)
28	evaporation of metals (vacuum not broken between adhesion layer and platinum)	electron beam evaporator (TRL)
29	acetone soak, with ultrasonic (for patterned wafers)	solvents wet bench (TRL)
30	rinse in acetone, methanol, then DI water (for patterned wafers)	solvents wet bench (TRL)
31	spin dryer: 140 sec. rinse + 240 sec. dry	spin dryer (TRL)
32	sinter at 650°C for one hour	tube furnace A3 (TRL)
	Membrane Release (Membrane Wafers Only)	
33	etch back side in KOH at 75°C for about 12 hours, while protecting front with one-side etch jig	fume hood (RGL)
34	rinse in DI water	fume hood (RGL)
	Deposition and Patterning of Nitride Passivation Layer (Nitride-Coated Wafers Only)	
35	PECVD deposition of 1000 Å nitride	PECVD-RIE system (TRL)
36	HMDS deposition	HMDS oven (TRL)
37	coat front of wafer with OCG 825 resist	coater (TRL)
38	prebake 30 min. at 90°C	prebake oven (TRL)
39	exposure of front side with coating mask (figure B-3), aligning to metal pattern	Karl Suss aligner 1 (TRL)

40	develop in OCG 934 1:1 developer (~90 sec)	solvents wet bench (TRL)
41	postbake 30 min. at 120°C	postbake oven (TRL)
42	etch away exposed nitride	PECVD-RIE system (TRL)
	Dicing Up Samples (All Wafers)	
43	dice wafer into samples	die saw (ICL)
44	acetone soak to remove die saw tape	fume hood (RGL)
45	rinse in acetone, rinse in methanol, rinse in DI water, blow dry	fume hood (RGL)
	Deposition and Patterning of Alumina Passivating Layer (Alumina-Coated Wafers Only)	
46	rinse in acetone, rinse in methanol, rinse in DI water, blow dry	fume hood (RGL)
47	3000 Å alumina evaporated onto samples	e-beam (General Vacuum[50])
48	rinse in acetone, rinse in methanol, rinse in DI water, blow dry	fume hood (RGL)
49	sample baked on hot plate at ~120°C for 30 min.	fume hood (RGL)
50	AZ P4620 photoresist painted on sample with toothpick, leaving edges and bond pads exposed	fume hood (RGL)
51	bake on hot plate at ~120°C for 30 min.	fume hood (RGL)
52	1 min. dip in BOE	fume hood (RGL)
53	rinse with DI water	fume hood (RGL)
54	remove photoresist with ~10 min. soak in acetone	fume hood (RGL)
55	rinse in acetone, rinse in methanol, rinse in DI water, blow dry	fume hood (RGL)

Appendix B

Mask Set

This appendix contains layout diagrams for the mask set used to fabricate the samples. The layout was made using KIC[51]. The masks are, in order, for:

- Patterning the back side nitride for use as a KOH etch mask
- Patterning the metal layer with image reversal
- Patterning the coating layer to allow access to the contact pads

An overlay of the three masks is also included to demonstrate how the layers overlap.

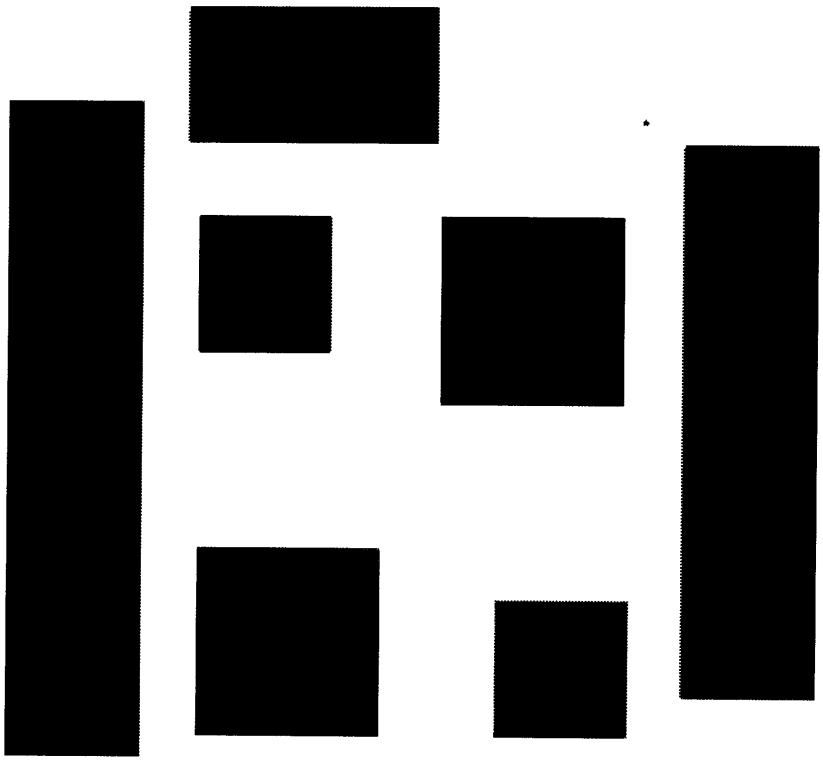

Figure B-1: Backside Nitride Layer Mask (dark field)
The small mark in the upper right-hand corner is for aligning to the metal layer

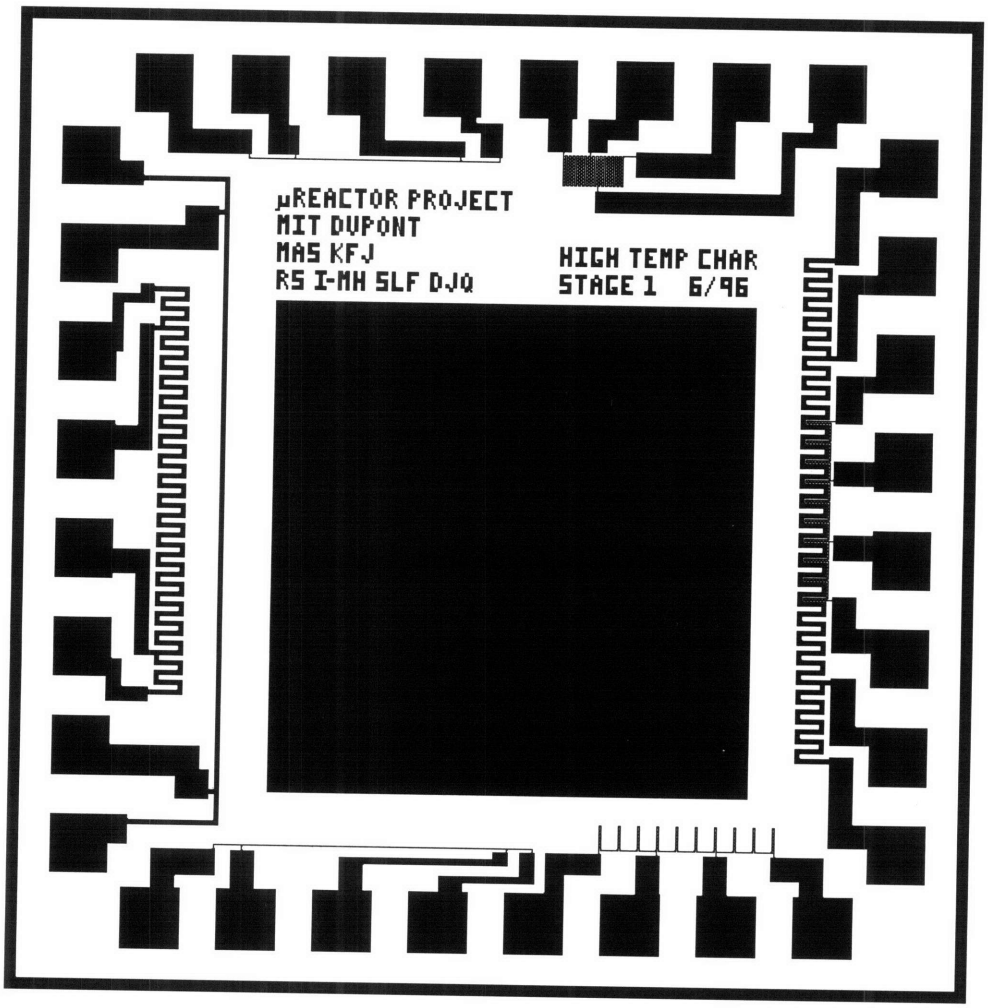

Figure B-2: Metal Pattern Mask (clear field)

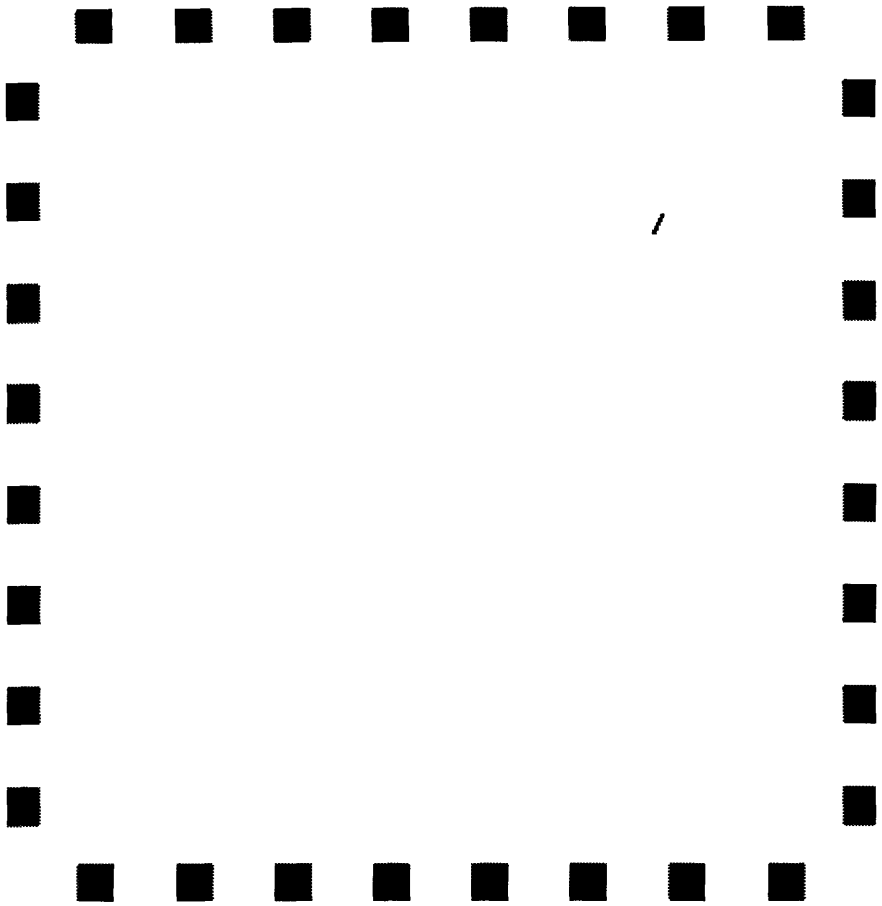

Figure B-3: Passivation Layer Mask (dark field)
The small mark in the upper right is for aligning to the metal layer

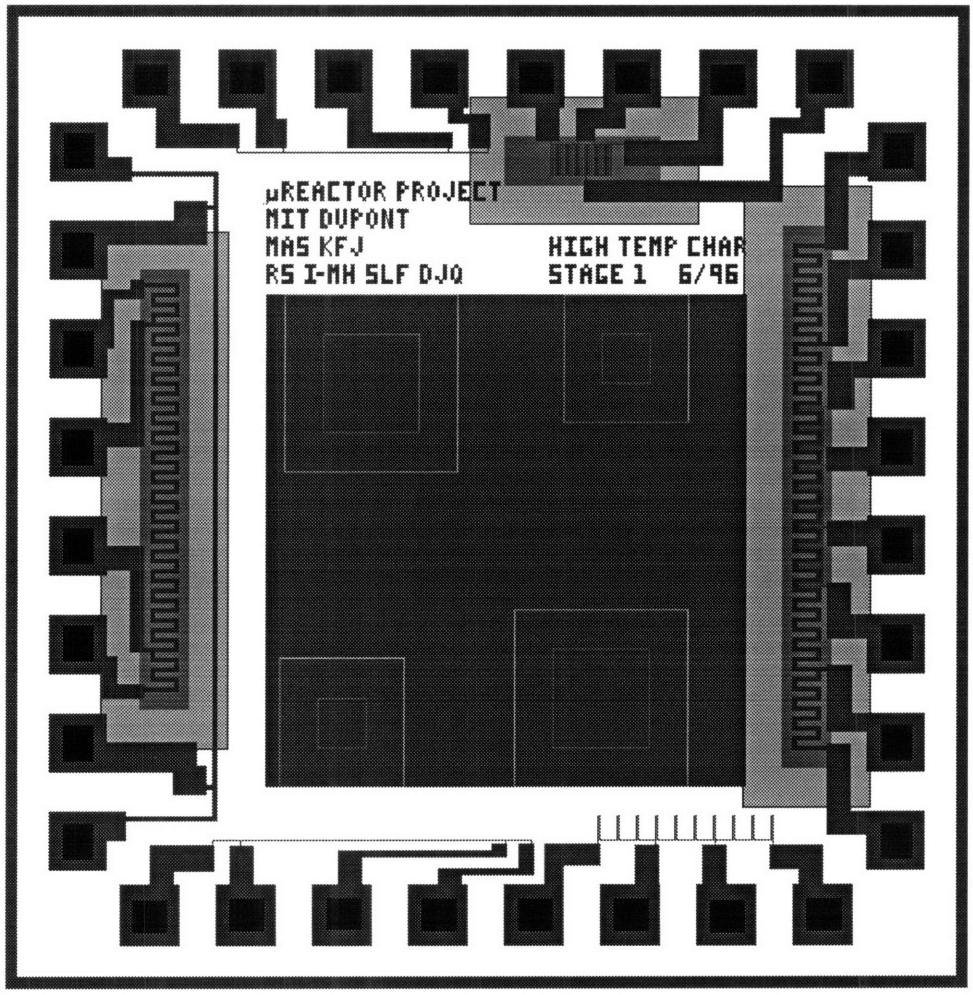

Figure B-4: The Complete Mask Set
The backside nitride mask is overlaid as a mirror image, and the membrane dimensions after the KOH etch are also shown.

Appendix C

Sample Packaging for In Situ Resistance Measurement

This appendix contains a detailed description of how the samples were packaged for the in situ resistance measurement described in section 2.3.

Mold Construction

1) Using a razor blade, a ~0.8" X 2" rectangle was cut out of a ~0.2"-thick wax sheet.
2) The sheet with the cut-out was placed on top of a second wax sheet.
3) The two sheets were fused together at the seams with a soldering iron.
4) A silicon chip was placed in the center of the resulting rectangular cavity, to create an indentation for holding samples.
5) With the soldering iron, all sharp corners were rounded, and a thin coating of wax was dripped over the silicon chip. The resulting mold is shown in figure C-1.

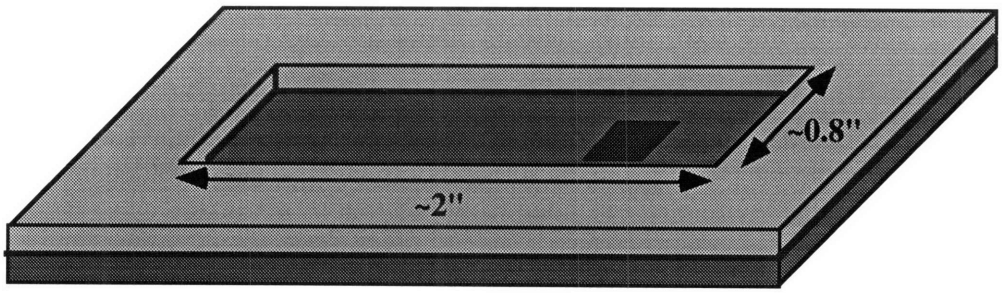

Figure C-1: Mold for Casting Base Plate

Base Plate Construction

1) The mold was coated with silicone spray.

2) ~25 grams of the Rescor® 780 Precision Castable Alumina Ceramic[52] powder were combined with ~6 grams of the activator solution to form a paste.

3) The paste was poured into the coated mold, and the mold was vibrated for ~10 minutes to release trapped air.

4) The ceramic was cured in air at room temperature for 24 hours.

5) The plate was released from the mold, by melting two holes through the back of the wax and pushing the plate out with toothpicks.

6) The plate was checked for fit (the complete jig must fit into a 1"-diameter tube), sanded, and cleaned with acetone to remove any remaining wax.

7) The plate was fired for one hour at 1100°C in the furnace.

8) The wax mold was repaired with a soldering iron and extra wax.

Manufacture of Contact Assembly

1) 5 , 11" segments cut from 0.02"- diameter Kanthal D® wire.

2) 10, 3" segments cut from wire-wrap wire, and the ends stripped.

3) Segments of wire wrap were wrapped loosely to both ends of the Kanthal® wire.

4) 5, 1/8" X 1/4" rectangles were cut with scissors out of a sheet of 0.001"-thick platinum foil.

5) For each of the 5 Kanthal® wires, the following process was repeated:

    a) The wire-wrap wire was spot-welded to the Kanthal® wire at one end.

    b) The other end of the wire assembly was threaded through a 12" alumina tube with a 1/16" inner diameter and a 1/8" outer diameter.

    c) Using the unwelded segment of wire-wrap wire, the ensemble was pulled forward until the weld joint between the wire wrap and the Kanthal® wire was about 1 1/2" inside the far end of the tube. The unwelded end of the Kanthal® wire now extended from the tube by about 1/2".

    d) The unwelded wire wrap is removed.

    e) In its place, a piece of platinum foil is spot welded to the Kanthal® wire tip. The resulting wire structure is shown in figure C-2.

6) The type-K (chromel-alumel) thermocouple wires were stripped, threaded through alumina tubes, and spot welded together at one end. The thermocouple extended out of the tubes by about 1/2".

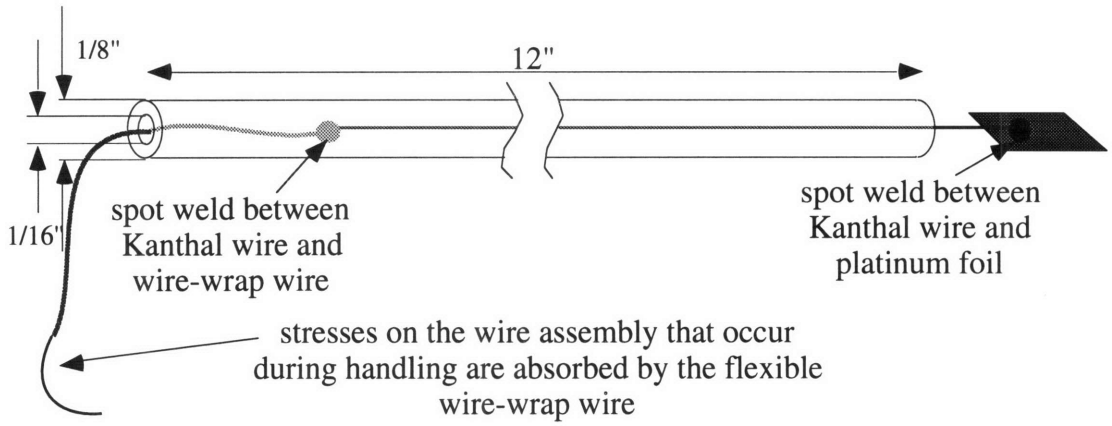

Figure C-2: Single Wire Tube After Assembly

Jig Assembly

1) The base plate was placed on a flat piece of foil or paper towel. The five wire tubes were laid down side by side in line with the plate, so that the platinum foil ends of the tubes extended over the base plate by ~1".

2) Water was added by eyedropper to ~20 grams of Omegabond® 600 High Temperature Chemical Set Cement[53] powder, until a paste with the consistency of toothpaste was formed.

3) The wire tubes were attached to eachother and to the base plate with the cement.

4) The thermocouple was cemented on top of the wire tubes, and the thermocouple tip bent down towards the sample indentation.

5) The other end of the thermocouple wires were attached to a male thermocouple plug (the mate to the female thermocouple plug which was attached to the temperature input of the programmable controller).

6) The structure was allowed to cure in air at room temperature for 24 hours.

7) The jig was brought slowly (~5 °/min) up to 1100°C in the furnace and fired for one hour.

Connecting to the Sample

1) The sample was placed in the indentation on the base plate, fastened down by drops of cement on the two corners away from the platinum foil pads, and then allowed to sit for ~1 hour in order to harden the cement "tacks".

2) The jig head was wrapped in aluminum foil, leaving the platinum pads and half of the sample exposed. The aluminum helped to distribute heat for the purposes of wedge bonding in the next step.

3) The jig was mounted on the wedge bonder stage, and heated to 350°C.

4) 0.001"-diameter platinum wire, that had previously annealed at 650°C for one hour in the furnace, was threaded through the wedge bonder.

5) Once the jig head had sat at 350°C for ~10 minutes, the platinum wire could be bonded between the platinum foil and the contact pads on the sample.

6) The jig was removed from the bonder and allowed to cool. Finally, the aluminum foil was removed. The complete jig assembly is shown in figure 2-2.

Bibliography

[1] J. J. Lerou, M. P. Harold, J. Ryley, J. Ashmead, T.C. O'Brien, M. Johnson, J. Perrotto, C. T. Blaisdell, T. A. Rensi, and J. Nyquist, "Microfabricated minichemical systems: techical feasibility," Microsystem Technology for Chemical and Biological Microreactors, DECHEMA Monographs, vol. 132, 1996, pp. 51.

[2]D. Hönicke and G. Weissmeier, "Heterogeneously catalyzed reactions in a microreactor," vol. 132, 1996, pp. 93.

[3] K.-P. Jäckel, "Microtechnology: application opportunities in the chemical industry," vol. 132, 1996, pp.29

[4] W. Ehrfield, v. Hessel, H. Möbius, T. Richter, K. Russow, "Potentials and realization of microreactors," ibid, vol. 132, 1996, pp. 1

[5] T.A. Ameel, R.O. Warrington, R. S. Wegeng, M. K. Drost, "Miniaturization technologies applied to energy systems," Proceedings of the 1996 Engineering Systems Design and Analysis Conference, Montpellier, France. vol. 1, pp. 123-134.

[6] R. Srinivasan, S.L. Firebaugh, I.-M. Hsing, J. Ryley, M. P. Harold, K. F. Jensen and M. A. Schmidt, "Chemical performance and high temperature characterization of micromachined chemical reactors," to be presented at Transducers '97, Chicago, 1997.

[7] S. M. Sze, *VLSI Technology*, 2nd edition, McGraw-Hill, New York, 1988, pp.375-421.

[8] J. W. Gardner, A. Pike, N. F. deRooij, M. Koudelka-Hep, P. A. Clerc, A. Hierlemann, W. Göpel, "Integrated array sensor for detecting organic solvents," Sensors and Actuators B, vol. 26-27, (1995), pp. 135-139.

[9] Chemical Rubber Company, *CRC Handbook of Chemistry and Physics*, CRC Press, Inc., Boca Raton, Florida; 1992.

[10] F. Maseeh, M. Arnone, and S. D. Senturia, "Mechanical properties of microelectronics thin films: silicon nitride (Si_3N_4)," MIT, VLSI Publications, VLSI Memo No. 89-576, October 1989.

[11] ASM International, *Binary Alloy Phase Diagrams*, 2nd ed., edited by Thaddeus B. Massalski, 1990.

[12] J. O. Olowolafe, R. E. Jones, Jr., A. C. Campbell, R. I. Hegde, C. J. Mogab, R. B. Gregory, "Effects of anneal ambients and Pt thickness on Pt/Ti and Pt/Ti/TiN interfacial reactions," J. Appl. Phys., vol. 73, no. 4, 15 February 1993, pp. 1764-1772.

[13] K.H. Park, C. Y. Kim, Y. W. Jeong, H. J. Kwon, K. Y. Kim, J. S. Lee, and S. T. Kim, "Microstructures and interdiffusions of Pt/Ti electrodes with respect to annealing in the oxygen ambient," J. Mater. Res., vol. 10, no. 7, Jul 1995, pp. 1790-1794.

[14] G. R. Fox, S. Trolier-McKinstry, and S. B. Krupanidhi, "Pt/Ti/SiO2/Si substrates," J. Mater. Res., vol. 10, no. 6, Jun 1995, pp. 1508-1515.

[15] K. Sreenivas, I. Reaney, T. Maeder, N. Setter, C. Jagadish, and R. G. Elliman, "Investigation of Pt/Ti bilayer metallization on silicon for ferroelectric thin film integration," J. Appl. Phys., vol. 75, no. 1, Jan 1994, pp. 232-239.

[16] P. D. Hren, H. Al-Shareef, S. H. Rou, A. I. Kingon, P. Buaud, and E. A. Irene, "Hillock formation in platinum films," Mat. Res. Soc. Symp. Proc., vol. 260, 1992, pp. 575-580

[17] S. R. Summerfelt, D. Kotecki, A. Kingon, and H. N. Al-Shareef, "Pt hillock formation and decay," Mat. Res. Soc. Symp. Proc., vol. 361, 1995, pp. 257-262.

[18] D. J. Eichorst and C. J. Baron, "Effects of platinum electrode structures on crystallinity and electrical properties of mod-prepared PZT capacitors," Mat. Res. Soc. Symp. Proc., vol. 310, 1993, pp. 201-208.

[19] M. Murakami, "Thermal strain in lead thin films II: Strain relaxation mechanisms," Thin Solid Films, vol. 55, 1978, pp. 101-111.

[20] P. Chaudhari, "Hillock growth in thin films," J. Appl. Phys., vol. 45, no. 10, Oct 1974, pp. 4339-4347.

[21] M. S. Jackson and C.-Y. Li, "Stress relaxation and hillock growth in thin films," Acta Metall., vol. 30, 1982, pp. 1993-2000.

[22] D. S. Gardner and P. A. Flinn, "Mechanical stress as a function of temperature in aluminum films," IEEE Transactions on Electron Devices, vol. 35, no. 12, Dec 1988, pp. 2160-2169.

[23] F. M. d'Heurle and P. S. Ho, "Electromigration in thin films," from *Thin Films- Interdiffusion and Reactions*, edited by J. M. Poate, K. N. Tu and J. W. Mayer, sponsored by the Electrochemical Society, Inc., John Wiley & Sons, New York, 1978, pp. 243-303.

[24] E. Jiran and C. V. Thompson, "Capillary instabilities in thin, continuous films," Thin Solid Films, vol. 208, 1992, pp. 23-28.

[25] W. W. Mullins, "Theory of thermal grooving," J. of Appl. Phys., vol. 28, no. 3, March, 1957, pp. 333-339.

[26] D. J. Srolovitz and M. G. Goldiner, "The thermodynamics and kinetics of film agglomeration," JOM, March 1995, pp. 31-36.

[27] D. J. Srolovitz, "On the stability of surfaces of stressed solids," Acta Metall., vol. 37, no. 2, pp. 621-625.

[28] S. K. Sharma and J. Spitz, "Hillock formation, hole growth and agglomeration in thin silver films," Thin Solid Films, vol. 65, 1980, pp. 339-350.

[29] Ravi Srinivasan, personal communication.

[30] The Kanthal Corporation, 119 Wooster Street, P. O. Box 281, Bethel, CT 06801.

[31] National Instruments Corporation, 6504 Bridge Point Parkway, Austin, TX 78730-5039.

[32] Quate, C. F., "The AFM as a tool for surface imaging," Surface Science, vol. 299-300, 1994, pp. 980-995.

[33] J.W. Mayer and J. M. Poate, "Depth profiling techniques," from *Thin Films-Interdiffusion and Reactions*, edited by J. M. Poate, K. N. Tu and J. W. Mayer, sponsored by the Electrochemical Society, Inc., John Wiley & Sons, New York, 1978, p. 145.

[34] Tencor Instruments, Mountain View, CA 94043.

[35] P. A. Flinn, D. S. Gardner, and W. D. Nix, "Measurement and interpretation of stress in aluminum-based metallization as a function of thermal history," IEEE Transactions on Electron Devices, Vol. ED-34, no. 3, March 1987, pp. 689-699.

[36] M. Ohring, *The Materials Science of Thin Films*, Academic Press, Inc., Boston, 1992, pp.95-96.

[37] P. Joubert, P. Auvray, A. Guivarc'h, and G. Pelous, "Growth of platinum silicide under protective layers," Applied Physics Letters, Vol. 31, No. 11, December 1977, pp. 753-755.

[38] S. Kirkpatrick, "Percolation and conduction," Reviews of Modern Physics, vol. 45, no. 4, October 1973, pp. 574-588.

[39] A. K. Ahmad and B. L. Evans, "A resistance network representation of electrical conduction in Pt and Cu films," Surface Science, vol. 364, 1996, pp. 39-53.

[40] D. A. G. Bruggeman, "Berechnung verschiedener physikalischer Konstanten von heterogenen Substanzen," Annalen der Physik, vol. 24, 1935, pp. 636-664.

[41] D. S. McLachlan, "Equation for the conductivity of metal-insulator mixtures," Journal of Physics C: Solid State Physics, vol. 18, 1985, pp. 1891-1897.

[42] G. L. Kellogg, "Temperature dependence of surface self-diffusion on Pt(001)," Surface Science, vol. 246, 1991, pp. 31-36.

[43] D. J. Srolovitz and S. A. Safran, "Capillary instabilities in thin films. I. Energetics," Journal of Applied Physics, vol. 60, no. 1, 1 July 1986, pp. 247-254.

[44] E. Jiran and C. V. Thompson, "Capillary instabilities in thin films," Journal of Electronic Materials, vol. 19, no. 11, 1990, pp. 1153-1160.

[45] G. L. Kellogg, T. T. Tsong, and P. Cowan, "Direct observations of surface diffusion and atomic interactions on metal surfaces," Surface Science, vol. 70, 1978, pp. 485-519.

[46] A. J. Learn, "Electromigration effects in aluminum alloy metallization," Journal of Electronic Materials, vol. 3, 1974, pp. 531-552.

[47] S. P. Murarka, E. Kinsbron, D. B. Fraser, J. M. Andrews, and E. J. Lloyd, "High temperature stability of PtSi formed by reaction of metal with silicon or by cosputtering," J. Appl. Phys., vol. 54, no. 12, Dec 1983, pp. 6943-6951.

[48] S. P. Murarka, *Silicides for VLSI Applications*, Academic Press, Inc., Ltd,. London, 1983, pp. 118-119.

[49] Karl Suss America Inc., Waterbury Center, Vermont 05677.

[50] General Vacuum, 198 Alpha Park, Cleveland, Ohio 44143.

[51] G. Billingsley and K. Keller, *KIC: A Graphics Editor for Integrated Circuits*, University of California at Berkeley.

[52] Cotronics Corporation, 3379 Shore Parkway, Brooklyn, New York 11235.

[53] Omega, One Omega Drive, Box. 4047, Stamford, Connecticut 06907-0047.